

Comparison between relativistic and nonrelativistic models of the nucleon-nucleon effective interaction.

I. Normal-parity isoscalar transitions

J. J. Kelly and S. J. Wallace

Department of Physics, University of Maryland, College Park, Maryland 20742

(Received 22 October 1993)

Relativistic density-dependent effective interactions for nucleon-nucleus scattering based upon a complete set of Lorentz-invariant NN amplitudes are used in calculations of elastic and inelastic scattering to normal-parity states of self-conjugate targets. Owing to distortion of Dirac spinors by the relativistic mean fields, the effective interaction appropriate for use in a Schrödinger formalism incorporates relativistic density dependence, which is stronger for inelastic than elastic scattering. The dominant effect for normal-parity transitions is equivalent to a short-ranged repulsive contribution to the real central interaction that is proportional to density and nearly independent of energy. Pauli blocking of occupied intermediate states is included and gives results similar to the familiar Clementel-Villi damping of the absorptive potential. The relativistic effective interaction is compared with nonrelativistic G -matrix calculations and with empirical effective interactions fitted to data for proton elastic and inelastic scattering. Calculations for elastic and inelastic scattering are compared with data for 200, 318, and 500 MeV and we find that the agreement with data improves as the energy increases. The density dependence of the relativistic model is much stronger at low energies than either the G matrix or the empirical interaction; its repulsive contribution to the central interaction is too strong to give a good description of the data for 200 MeV. Near 500 MeV the relativistic interaction is closer to the empirical interaction and better agreement with the data is obtained, whereas the density dependence of nonrelativistic effective interactions is too small.

PACS number(s): 25.40.Cm, 25.40.Ep, 24.10.Jv

I. INTRODUCTION

Considerable progress has been made in both relativistic and nonrelativistic theories of nucleon elastic and inelastic scattering by nuclei. The most successful nonrelativistic calculations of nucleon scattering are based upon the local-density approximation (NRLDA) and employ effective interactions based upon a Brueckner G matrix constructed for infinite nuclear matter [1–8]. Thus, density-dependent corrections due to Pauli blocking and to propagation in the mean field are included. A recent NRLDA calculation, due to Ray [8], indicates that these effects remain important for energies as high as 800 MeV, and hence should be included in relativistic calculations also. However, these approaches include relativistic effects only in the kinematics, and do not handle distortion of Dirac spinors or boosts.

Calculations based upon the Dirac equation handle the relativistic properties of the spinors properly and provide a very successful model for elastic scattering, especially for spin observables [9]. Global scalar and vector potentials with simple geometries provide accurate fits to the elastic scattering data over a broad energy range [10,11]. When reduced to Schrödinger-equivalent form, the real central potential develops the so-called “wine-bottle” shape for energies below 300 MeV. In NRLDA models this feature is attributed to the density dependence of the effective interaction. Similar results are obtained from the relativistic impulse approximation (RIA) in which the NN interaction is expanded in terms of

Lorentz invariants and folded with Lorentz scalar and vector densities for the target [12–15]. Even without explicit density dependence, the Schrödinger-equivalent real central optical potentials that emerge from the RIA also display the wine-bottle shape. The ρ^2 contributions to RIA potentials have been interpreted as the effect of virtual $N\bar{N}$ pairs in the medium [16]. More recent versions of the RIA model now include the complete set of Lorentz invariants [17,18], but usually do not include the Pauli blocking and self-energy corrections known to be important for energies below 300 MeV [19]. Murdock and Horowitz [20] applied Pauli blocking corrections to the absorptive potential in RIA calculations for elastic scattering, but did not include the self-energy corrections which Ray demonstrates are important to the real part of the central interaction for energies up to 800 MeV.

Although the Dirac models of proton elastic scattering have proven quite successful for energies above 300 MeV, particularly in the description of spin observables, few inelastic scattering calculations have been performed using Dirac models. Early versions of the relativistic impulse approximation have been used with transition densities either from electron scattering or from a relativistic RPA model, but did not include all the Lorentz invariants required for a complete description of the NN amplitude [21–24]. Collective model [25] and coupled-channels calculations [26,27] have been performed by deforming optical potentials from Dirac phenomenology. No calculations have been reported to date that include both the complete set of Lorentz invariants and a relativistic model of nuclear structure.

Furnstahl and Wallace [28] have constructed an effective interaction based upon the IA2 version of the relativistic impulse approximation. The IA2 model uses a complete set of Lorentz invariants based upon a meson-exchange analysis of nucleon-nucleon scattering. The effective interaction incorporates the distortions of the Dirac spinors required by a relativistic treatment based upon the Dirac equation and includes differences between scalar and vector densities. This procedure is similar to but more complete than the m^* approximation to Dirac spinors. Since spinor distortion depends upon nuclear density, the effective interaction includes density dependence due to relativistic effects even without including traditional Pauli blocking or dispersion corrections. The dominant effect of this relativistic density dependence is equivalent to a short-ranged repulsive contribution to the real central interaction that is proportional to density and nearly independent of energy [19,29]. The effective interaction for elastic scattering involves the distortion of three spinors, whereas for inelastic scattering four spinors must be distorted. Thus the density dependence is stronger for the inelastic interaction than for the elastic interaction. This enhancement of inelastic density dependence is similar to the rearrangement contribution predicted by Cheon *et al.* [30,31], but is not as simple as the $(1 + \rho\partial/\partial\rho)$ factor that emerges from their schematic model.

For elastic scattering, the IA2 effective interaction can be used to perform folding-model calculations with the Schrödinger equation that reproduce the IA2 results with the Dirac equation [28]. The IA2 effective interaction has also been used by Ray to investigate elastic scattering by a polarized target [32]. For inelastic scattering, the IA2 effective interaction makes it possible to extend the relativistic impulse approximation to a variety of nuclear transitions and permits employment of transition densities available from electron scattering. This approach, employed here, has the advantage over previous RIA calculations of avoiding the need for a relativistic nuclear structure model, for which good densities for inelastic transitions are not generally available. It is predictive in the sense that no adjustable parameters are available for fitting nucleon-nucleus data.

An empirical effective interaction, based upon the properties of the G matrix, has been used to analyze proton elastic and inelastic scattering data systematically [33,34]. Medium modifications to the t matrix are expanded in a linear series and the coefficients are fitted to data for many transitions in several nuclei simultaneously. Consistency between elastic and inelastic scattering requires stronger density dependence in the inelastic interaction and this can be achieved using the Cheon rearrangement factor [30] to relate the inelastic and elastic interactions. Use of data for states with transition densities of either surface character or with strong interior lobes endows the procedure with good sensitivity to the density dependence of the effective interaction. Comparisons between interactions fitted to transitions within several nuclei, either independently or simultaneously, demonstrate that the empirical effective interaction depends primarily upon local density and is essentially in-

dependent of either state or nucleus, thus confirming the basic properties of the local-density hypothesis.

Empirical effective interactions (EEI) have been constructed for several energies between 135 and 650 MeV [34–40]. Between about 100 and 200 MeV we find that the density dependence of the EEI is similar to that of the G matrix, and perhaps somewhat smaller than estimated by some of the nuclear matter calculations. However, we find that interaction strengths at low density must be reduced more than required by the LDA to reproduce data for surface-peaked transition densities [34–36]. These observations can be interpreted as evidence that medium modifications are stronger at the surface and weaker in the interior of finite nuclei than for infinite nuclear matter of corresponding local density. We also find that at 200 MeV the absorptive potential for the EEI interaction is considerably weaker than that of the IA2 interaction without Pauli blocking. By contrast, for energies above 300 MeV we find that the density-dependent repulsive contribution to the real central interaction is considerably stronger than predicted by the NRLDA and that density-dependent corrections to the absorptive potential are weaker at 300 MeV and opposite in sign at 500 MeV than expected from Pauli blocking [37–39]. On the other hand, optical potentials computed from the empirical effective interaction for energies above 300 MeV are similar to those from the IA2 model. Most notably, the strong repulsive contribution to the IA2 real central interaction is close to that which emerges from phenomenological analysis of the data above 300 MeV. These comparisons suggest that the phenomenological analyses are observing relativistic effects for $E_p \geq 300$ MeV and that the relativistic impulse approximation for lower energies could benefit from inclusion of G -matrix corrections.

Our calculations employ the IA2 effective interaction of Furnstahl and Wallace and an extended IA2 interaction which includes Pauli blocking of intermediate states. Calculations of elastic and inelastic scattering to normal-parity states of self-conjugate targets are extended down to 200 MeV. Such cases offer the possibility of using transition densities from electron scattering to minimize uncertainties due to nuclear structure and to thereby isolate the effective interaction for study. Future work will consider abnormal-parity and charge-exchange transitions. The relativistic effective interactions used are compared with the nonrelativistic G matrix and the empirical effective interaction in Sec. II. Results for elastic scattering from ^{16}O and ^{40}Ca at 200, 318, and 500 MeV are compared with the data in Sec. III. Results for inelastic scattering to selected states of ^{16}O and ^{40}Ca are compared with data for the same energies in Sec. IV. Discussion of these results is given in Sec. V and a summary of our conclusions is given in Sec. VI.

II. MODELS OF THE EFFECTIVE INTERACTION

A. Representations of the effective interaction

The nucleon-nucleon interaction in the nucleon-nucleus (NA) center of mass frame can be represented in the form

[41,42]

$$\begin{aligned}
t_{\text{eff}} = & t_{00}^C + t_{\tau}^C \boldsymbol{\tau}_1 \cdot \boldsymbol{\tau}_2 + t_{\sigma}^C \boldsymbol{\sigma}_1 \cdot \boldsymbol{\sigma}_2 + t_{\sigma\tau}^C \boldsymbol{\sigma}_1 \cdot \boldsymbol{\sigma}_2 \boldsymbol{\tau}_1 \cdot \boldsymbol{\tau}_2 \\
& + it_0^{LS} (\boldsymbol{\sigma}_1 + \boldsymbol{\sigma}_2) \cdot \hat{\mathbf{n}} + it_{\tau}^{LS} (\boldsymbol{\sigma}_1 + \boldsymbol{\sigma}_2) \cdot \hat{\mathbf{n}} \boldsymbol{\tau}_1 \cdot \boldsymbol{\tau}_2 \\
& + t_0^{TND} S_{12}(\hat{\mathbf{q}}) + t_{\tau}^{TND} S_{12}(\hat{\mathbf{q}}) \boldsymbol{\tau}_1 \cdot \boldsymbol{\tau}_2 \\
& + t_0^{TNX} S_{12}(\hat{\mathbf{Q}}) + t_{\tau}^{TNX} S_{12}(\hat{\mathbf{Q}}) \boldsymbol{\tau}_1 \cdot \boldsymbol{\tau}_2, \quad (1)
\end{aligned}$$

where $\mathbf{q} = \mathbf{k}_i - \mathbf{k}_f$ is the direct momentum transfer, $\mathbf{Q} = \mathbf{k}_i + \mathbf{k}_f$ is the exchange momentum transfer, $\hat{\mathbf{n}} = \mathbf{q} \otimes \mathbf{Q} / |\mathbf{q} \otimes \mathbf{Q}|$ is the unit normal to the scattering plane, and $S_{12}(\hat{\mathbf{q}}) = 3\boldsymbol{\sigma}_1 \cdot \hat{\mathbf{q}} \boldsymbol{\sigma}_2 \cdot \hat{\mathbf{q}} - \boldsymbol{\sigma}_1 \cdot \boldsymbol{\sigma}_2$ is the two-body tensor operator. Each interaction component is considered to be a function of both momentum transfer q and local density ρ . To simplify the formulas for constructing spin-orbit scattering potentials, it is convenient to introduce the auxiliary form

$$t'^{LS} = -\frac{2}{qQ} t^{LS} = -(k^2 \sin \theta)^{-1} t^{LS}. \quad (2)$$

To compare various models of the effective interaction, it is often convenient to use the parametrization which was introduced in Refs. [33,34]:

$$\begin{aligned}
t_i(q, \kappa_F) = & (S_i - d_i \kappa_F^{\alpha_i}) t_i^{(f)}(q) \\
& + \kappa_F^{\gamma_i} q^{\delta_i} \sum_{n=1}^N a_{in} y^{\beta_i}(q/\mu_{in}). \quad (3)
\end{aligned}$$

Here, $\kappa_F = k_F/1.33$ represents the local Fermi momentum relative to saturation, $t^{(f)}(q)$ is the free interaction at zero density, $y(x) = (1 + x^2)^{-1}$ is a Yukawa function, and the μ_{in} are various mass parameters which are chosen to optimize the fit to component i . Theoretical interactions require the scale factors S_i to be unity, although the scale factors may be allowed to vary in empirical analyses of scattering data. If the individual components of the interaction are interpreted as Fourier transforms of Yukawa potentials [33], one finds that the natural exponents β are 1 for central, 2 for spin-orbit, and 3 for tensor interactions. Similarly, $\delta = 2$ for tensor interactions and $\delta = 0$ otherwise. For the spin-orbit components of the interaction, we apply this parametrization to t'^{LS} .

The parametrization given in Eq. (3) applies to the real and imaginary parts of each component of the effective interaction separately. The ranges and exponents are chosen such that good fits to theoretical effective interactions are obtained with a small number of strength or damping parameters, a or d , for each component. Although the representation given in Eq. (3) can be used to fit the density dependence of any component of the effective interaction to nucleon scattering data, so far only data for normal-parity isoscalar transitions dominated by the spin-independent central and spin-orbit interactions have been analyzed in detail. Hence it is convenient to number the $\text{Re}t_{00}^C$, $\text{Im}t_{00}^C$, $\text{Re}t_0^{LS}$, and $\text{Im}t_0^{LS}$ components as $i = 1, 4$.

1. Nonrelativistic effective interactions

Equation (3) has been used to parametrize the density dependence of the three nonrelativistic calculations

of the effective interaction that have been reported for energies above 200 MeV. The Paris-Hamburg effective interaction (PH) was constructed by von Geramb and collaborators [5,6] using the Paris potential [43] and a generalization [3,4] of the Siemens averaging procedure [44] to represent the effects of Pauli blocking and dispersion upon the correlated pair wave function in nuclear matter. The Nakayama-Love (NL) interaction [7] was constructed from the Bonn potential [45] and was designed to reproduce on-shell elements of the G matrix. The effective interaction due to Ray (LR) [8] used a coupled-channels nucleon-isobar model [46–48] and included Pauli blocking and binding potentials but did not include the nucleon optical potential in the propagator. To use the LR model we parametrize its density dependence and then replace its free interaction, which is not sufficiently accurate, with the Franey-Love (FL) t matrix [42]. Detailed comparisons between these interactions can be found in Refs. [33–39].

The parameters which represent these effective interactions according to the prescription of Eq. (3) are collected in Table I. To facilitate direct comparisons between the parameters for these models, we use the same choices of ranges and exponents for each, although more accurate fits to one or another of the theoretical interactions can sometimes be achieved with different choices. Also note that the free interactions for each of these models are different and that these differences do affect the scattering calculations. These differences also complicate comparisons between the models and are often larger than expected from uncertainties in the NN t matrix. Provided that the appropriate free interactions are used for each model, the parametrized effective interactions produce scattering calculations that are almost indistinguishable from the original interactions. Nevertheless, our calculations employ the original interactions, with the aforementioned exception for the LR model.

The density dependence of the real central part of the interaction is best described by the addition of a short-ranged repulsive core, due to the anticorrelation between identical nucleons, which enhances the differential cross section at large momentum transfer. The amplitude of the core contribution is proportional to the density, such that $\gamma_1 = 3$ in Eq. (3). The effect upon the real spin-orbit component is qualitatively similar. The primary effect of Pauli blocking upon the imaginary central part of the interaction can be described by a multiplicative damping factor which suppresses the forward cross section. The qualitative behavior of this effect is described well by the simple phase-space model due to Clementel and Villi [49], which predicts $\alpha_2 = 2$ and $d_2 \propto E_0^{-1}$.

2. Empirical effective interactions

Empirical interactions can be obtained by fitting the parameters of Eq. (3) to proton scattering data, but correlations among the parameters generally necessitate the use of a somewhat simpler parametrization which retains the most important features of the density dependence while minimizing correlations among the fitted parameters.

TABLE I. Parametrization of NRLDA interactions.

E (MeV)	t_i	$[\alpha\gamma\beta\delta]$	Coefficient	μ^a	PH	NL	LR
200	Ret_{00}^C	[3310]	a_{11} (MeV fm ³)	0	-61.5	13.7	-69.0
			a_{12} (MeV fm ³)	3.0	142.0	14.9	109.5
	Imt_{00}^C	[2210]	d_2		0.286	0.454	0.457
			a_{21} (MeV fm ³)	0	-11.8	-5.69	-7.37
	$\text{Ret}'_{00}{}^{LS}$	[3320]	a_{31} (MeV fm ⁵)	2.0	-9.49	-10.9	-8.01
			a_{32} (MeV fm ⁵)	4.0	6.57	5.28	5.69
	$\text{Imt}'_{00}{}^{LS}$	[2220]	a_{41} (MeV fm ⁵)	2.0	5.13	7.93	2.59
			a_{42} (MeV fm ⁵)	4.0	-3.78	-2.42	-2.45
320	Ret_{00}^C	[3310]	a_{11} (MeV fm ³)	0	-23.1	11.1	-38.9
			a_{12} (MeV fm ³)	3.0	83.3	17.6	100.1
	Imt_{00}^C	[2210]	d_2		0.151	0.285	0.263
			a_{21} (MeV fm ³)	0	-16.9	-10.2	0.83
	$\text{Ret}'_{00}{}^{LS}$	[3320]	a_{31} (MeV fm ⁵)	2.0	-5.35	-5.28	-4.92
			a_{32} (MeV fm ⁵)	4.0	3.88	2.73	4.26
	$\text{Imt}'_{00}{}^{LS}$	[2220]	a_{41} (MeV fm ⁵)	2.0	1.89	2.00	-1.70
			a_{42} (MeV fm ⁵)	4.0	-1.28	0.17	0.63
500	Ret_{00}^C	[3310]	a_{11} (MeV fm ³)	0			-35.1
			a_{12} (MeV fm ³)	3.0			108.3
	Imt_{00}^C	[2210]	d_2				0.174
			a_{21} (MeV fm ³)	0			-4.65
	$\text{Ret}'_{00}{}^{LS}$	[3320]	a_{31} (MeV fm ⁵)	2.0			-2.10
			a_{32} (MeV fm ⁵)	4.0			2.45
	$\text{Imt}'_{00}{}^{LS}$	[2220]	a_{41} (MeV fm ⁵)	2.0			-2.09
			a_{42} (MeV fm ⁵)	4.0			0.74

^aAn entry of 0 is used to indicate $\mu^{-1} = 0$ fm; otherwise, μ is given in units of fm⁻¹.

ters. Thus, the simplified parametrization [34]

$$\text{Ret}_{00}^C(q, \kappa_F) = S_1 \text{Ret}_{00}^{C(f)}(q) + b_1 \kappa_F^3 y(q/\mu_1), \quad (4a)$$

$$\text{Imt}_{00}^C(q, \kappa_F) = [S_2 - d_2 \kappa_F^2] \text{Imt}_{00}^{C(f)}(q), \quad (4b)$$

$$\text{Ret}'_{00}{}^{LS}(q, \kappa_F) = S_3 \text{Ret}'_{00}{}^{LS(f)}(q) + b_3 \kappa_F^3 y^2(q/\mu_3) \quad (4c)$$

yields more stable fits to scattering data than the full form, Eq. (3). However, it is also important to observe that accurate fits to data for states with surface-peaked transition densities can only be obtained if the scale factors (S_1 , S_2 , S_3) are allowed to vary, particularly for low energies. Usually, the imaginary spin-orbit component is too weak to be fitted and is constrained to its theoretical form. The range parameters μ_1 and μ_3 used for data analysis are usually based upon the most successful nuclear matter calculation for the same energy.

To facilitate comparison of the energy dependencies of the EEI and IA2 interactions, several new EEI analyses have been performed. Since the early EEI fits did not include elastic scattering data and were based upon the PH interaction instead of the free t matrix, those analyses were repeated including elastic scattering and using the FL t matrix to represent the interaction at zero density. The range parameters were based upon fits to the LR effective interaction. Components of the effective interaction that were not fitted, notably $\text{Imt}'_{00}{}^{LS}$, were taken

from the LR interaction for $E_p \geq 200$ MeV or PH for $E_p < 200$ MeV. The interactions use data for ¹⁶O at 135 MeV, both ¹⁶O and ²⁸Si at 180 MeV, both ¹⁶O and ⁴⁰Ca at 200, 318, and 500 MeV, and all three nuclei at 650 MeV. These results are collected in Table II. The fits for 200, 318, and 650 MeV were reported previously in Refs. [36], [38], and [40], respectively. The fit for 500 MeV is similar to that labeled EI-1 in Ref. [39], which was fitted to inelastic scattering data for ¹⁶O, but includes data for elastic scattering and for ⁴⁰Ca also.

3. Relativistic effective interactions

Four versions of the IA2 interaction have been produced: both elastic and inelastic effective interactions with and without Pauli blocking corrections. The formalism for construction of effective interactions without Pauli blocking was presented in Ref. [28]. Pauli blocking has been included by modifying the integration over relative momentum in the NN t matrix to include the angle-averaged Pauli blocking factor. Several technical improvements were made in the calculations and the NN amplitudes were updated using the recent SM93 phase-shift solution from Arndt's SAID program [50]. The calculations of Ref. [28] have been extended to include projectile energies of 200, 318, 500, 650, and 800 MeV. The interactions given in Ref. [28] did not include recoil corrections, causing the interaction at zero density to differ

TABLE II. Interactions in EEI form. The EEI fits use $\mu_1 = 1.5 \text{ fm}^{-1}$ for $E_p \leq 200 \text{ MeV}$ and $\mu_1 = 2.0 \text{ fm}^{-1}$ for $E_p > 200 \text{ MeV}$. The IA2 uses $\mu_1 = 2.0 \text{ fm}^{-1}$ and includes the short-range contribution to $\text{Im}t_{00}^C$ by modifying d_2 according to Eq. (5). Both EEI and IA2 use $\mu_3 = 6.0 \text{ fm}^{-1}$.

E (MeV)	Label	S_1	b_1	S_2	d_2	S_3	b_3
135	EEI	0.842	63.4	0.803	0.368	0.783	6.68
180	EEI	0.850	61.7	0.831	0.260	0.827	4.78
200	EEI	0.795	56.7	0.768	0.222	0.833	2.31
	IA2	1.0	180.5	1.0	0.314	1.0	5.31
318	EEI	1.136	131.9	1.031	-0.059	0.810	6.07
	IA2	1.0	175.7	1.0	0.126	1.0	2.62
500	EEI	1.245	160.9	0.960	-0.209	0.789	5.22
	IA2	1.0	173.1	1.0	0.006	1.0	1.43
650	EEI	1.0	162.8	0.89	-0.20	0.70	6.56
	IA2	1.0	167.4	1.0	-0.023	1.0	0.90
800	IA2	1.0	155.4	1.0	-0.040	1.0	0.49

somewhat from the free t matrix. In this work, the interactions were evaluated for both ^{16}O and ^{40}Ca ; although the recoil corrections are relatively small, their effects upon scattering calculations are not negligible. To facilitate comparisons with other models of the effective interaction and to remove most of the target dependence, we display interactions for ^{40}Ca with the Moller factor divided out, but always employ the appropriate interaction for scattering calculations.

The components of the IA2 effective interaction for ^{40}Ca most relevant to normal-parity isoscalar transitions are illustrated in Figs. 1–6. The symbols represent the interactions for $k_F = 0.0, 1.0,$ and 1.4 fm^{-1} and the lines represent fits to the interaction made with the

parametrization given in Eq. (3). The parameters are given in Table III. This parametrization gives good descriptions of the central components of the IA2 interaction with parameters that are stable and smooth. The Ret_0^{LS} components are also described well; however, although the two Yukawa coefficients are not separately well-determined, the sum of these coefficients is stable and smooth. Finally, the density dependence of the $\text{Im}t_0^{LS}$ component appears to be more complicated for the IA2 interaction than for the NRLDA interactions, particularly at low energies and for inelastic interactions, and is not represented as well by this simple parametrization, but fortunately this component is the least important for the present application.

TABLE III. Parametrization of IA2 interactions.

E (MeV)	t_i	$[\alpha\gamma\beta\delta]$	Coefficient	μ^a	Elastic	+PB	Inelastic	+PB
200	Ret_{00}^C	[3310]	a_{11} (MeV fm ³)	0	-82.1	-78.3	-147.2	-158.0
			a_{12} (MeV fm ³)	3.0	247.7	250.9	397.4	424.2
	$\text{Im}t_{00}^C$	[2210]	d_2		0.149	0.455	0.166	0.473
			a_{21} (MeV fm ³)	0	-19.9	-28.4	-27.4	-35.2
	Ret_0^{LS}	[3320]	a_{31} (MeV fm ⁵)	2.0	3.09	-3.12	4.01	-2.39
			a_{32} (MeV fm ⁵)	4.0	4.77	8.19	13.2	17.7
	$\text{Im}t_0^{LS}$	[2220]	a_{41} (MeV fm ⁵)	2.0	4.43	5.35	8.95	9.29
			a_{42} (MeV fm ⁵)	4.0	-1.48	-1.55	-6.56	-5.80
318	Ret_{00}^C	[3310]	a_{11} (MeV fm ³)	0	-87.1	-86.2	-150.7	-161.8
			a_{12} (MeV fm ³)	3.0	241.2	255.9	386.9	421.6
	$\text{Im}t_{00}^C$	[2210]	d_2		0.127	0.290	0.121	0.281
			a_{21} (MeV fm ³)	0	-28.6	-36.5	-41.1	-48.8
	Ret_0^{LS}	[3320]	a_{31} (MeV fm ⁵)	2.0	3.98	0.93	5.85	2.16
			a_{32} (MeV fm ⁵)	4.0	0.43	3.02	4.29	7.87
	$\text{Im}t_0^{LS}$	[2220]	a_{41} (MeV fm ⁵)	2.0	2.10	0.88	4.39	2.96
			a_{42} (MeV fm ⁵)	4.0	-1.31	-0.39	-4.68	-3.55
500	Ret_{00}^C	[3310]	a_{11} (MeV fm ³)	0	-101.8	-92.8	-175.1	-168.6
			a_{12} (MeV fm ³)	3.0	255.2	261.8	414.1	426.8
	$\text{Im}t_{00}^C$	[2210]	d_2		0.102	0.157	0.084	0.135
			a_{21} (MeV fm ³)	0	-35.0	-43.6	-47.2	-57.0
	Ret_0^{LS}	[3320]	a_{31} (MeV fm ⁵)	2.0	3.87	1.70	5.72	2.79
			a_{32} (MeV fm ⁵)	4.0	-0.83	1.16	1.08	3.78
	$\text{Im}t_0^{LS}$	[2220]	a_{41} (MeV fm ⁵)	2.0	0.96	1.19	1.89	2.24
			a_{42} (MeV fm ⁵)	4.0	-0.89	-1.05	-2.81	-3.11

^aAn entry of 0 is used to indicate $\mu^{-1} = 0 \text{ fm}$; otherwise, μ is given in units of fm^{-1} .

To facilitate comparison with the empirical effective interaction, Table II gives a simpler representation of the elastic IA2 effective interaction, including Pauli blocking, based upon the parametrization used previously for data analysis, Eqs. (4a)–(4c). The b_1 and b_3 parameters were estimated by fitting the relevant parametrizations to the IA2 interaction for $0 \leq q \leq 3 \text{ fm}^{-1}$. The range parameters $\mu_1 = 2.0 \text{ fm}^{-1}$ and $\mu_3 = 6.0 \text{ fm}^{-1}$ chosen for the phenomenological analyses give adequate representations of the IA2 interactions, although the IA2 inelastic spin-orbit interactions prefer a somewhat smaller value for μ_3 . Since the empirical effective interaction does not use the a_{21} parameter, which is significant for the IA2 interaction, we include its effect at $q \approx 0$ using

$$d_2 \longrightarrow d_2 - \frac{a_{21}}{\text{Im}t_{00}^C(0,0)} \quad (5)$$

in the simplified parametrization presented in Table II. Although the simpler parametrization does not represent the IA2 interaction as accurately as the full parametrization, it does permit qualitative comparisons with the phenomenology to be made more easily and simplifies the discussion of the energy dependence of medium modifications to the interaction. Note that all nucleon-nucleus scattering calculations with the IA2 interaction employ the original interaction rather than either of these parametrizations. Also note that the elastic interactions which include Pauli blocking should be most directly comparable to the nonrelativistic and empirical interactions listed in Tables I and II.

Similar results for the elastic interaction without Pauli blocking were obtained in Ref. [29] by fitting the parameters of Eqs. (4a)–(4c) directly to the Schrödinger equivalent optical potentials from the IA2 results of Ref. [19].

B. Properties of the effective interaction

1. $E_p = 200 \text{ MeV}$

The isoscalar spin-independent central and isoscalar spin-orbit components of the IA2 effective interactions for 200 MeV are shown in Figs. 1 and 4, respectively. The density dependence of the real central component may be described as a repulsive interaction that is proportional to density. Similar results are obtained from nonrelativistic theories of the effective interaction in nuclear matter, but for the nonrelativistic interactions the strength of this repulsive contribution is substantially smaller at this energy. The repulsion fitted to elastic and inelastic scattering data for ^{16}O and ^{40}Ca is also much smaller than predicted by the IA2 model. Similarly, the density dependence of the real spin-orbit interaction may be described by a short-range component proportional to density which is similar to but somewhat stronger than found in nonrelativistic models. Pauli blocking has very little effect upon these real components of the effective interaction.

Without Pauli blocking the density dependence of the imaginary central component is quite modest, but Pauli blocking produces a substantial damping of the absorp-

tive potential at low momentum transfer that is well described by the Clementel-Villi prescription. The damping coefficient is similar to that from nonrelativistic nuclear matter calculations and to the empirical effective interaction. However, a substantial short-range contribution is also required to reproduce the IA2 $\text{Im}t_{00}^C$ component at high momentum transfer; this contribution is stronger than in the nonrelativistic models and was omitted from the phenomenological analyses (compare coefficient a_{21} in Tables I–III). Although the imaginary spin-orbit interaction is weak at 200 MeV, its density dependence is relatively large but rather insensitive to Pauli blocking. The density dependence of the $\text{Im}t_0'^{LS}$ component is also similar to the predictions of nonrelativistic nuclear matter calculations, but this component is weak and cannot be determined very well by phenomenological analysis.

For the inelastic interactions, the distortion of the outgoing spinors nearly doubles the density dependence of the real central and the spin-orbit components. This effect is qualitatively similar to the $(1 + \rho\partial/\partial\rho)$ rearrangement effect predicted by Cheon *et al.* based upon self-consistency arguments [30,31]. According to the Cheon model a density-dependent contribution to the elastic interaction that is proportional to k_F^n is multiplied by $(3+n)/n$ for the inelastic interaction. This relationship is incorporated in the phenomenology of the empirical effective interaction and has been shown to be indispensable to the consistency between elastic and inelastic scattering. Although the relationship between the elastic and inelastic IA2 interactions need not necessarily conform to this simple prescription, the results listed in Table III demonstrate that it nonetheless applies to the aforementioned real components quite well. However, there is little difference between the imaginary central components of the elastic and inelastic IA2 interactions, contrary to the factor of $\frac{5}{3}$ that would be expected from the Cheon prescription. Also note that the relationship between the elastic and inelastic IA2 interactions is essentially unaffected by Pauli blocking.

Therefore, although the density dependencies for normal-parity isoscalar components of the nucleon-nucleon effective interaction at 200 MeV are qualitatively similar for relativistic and nonrelativistic models, there are two important differences. Firstly, the density dependence of the real central and spin-orbit components are substantially stronger in the IA2 model. Secondly, the density dependence of the imaginary central component is not enhanced for the inelastic interaction, in contrast to the Cheon rearrangement prescription.

2. $E_p = 318 \text{ MeV}$

The isoscalar spin-independent central and isoscalar spin-orbit components of the IA2 effective interactions for 318 MeV are shown in Figs. 2 and 5, respectively. Although the zero-density interaction changes, the density-dependent contribution to the real central component is almost unchanged from 200 MeV, whereas the density dependence of the real spin-orbit interaction decreases with increasing energy. For these components the re-

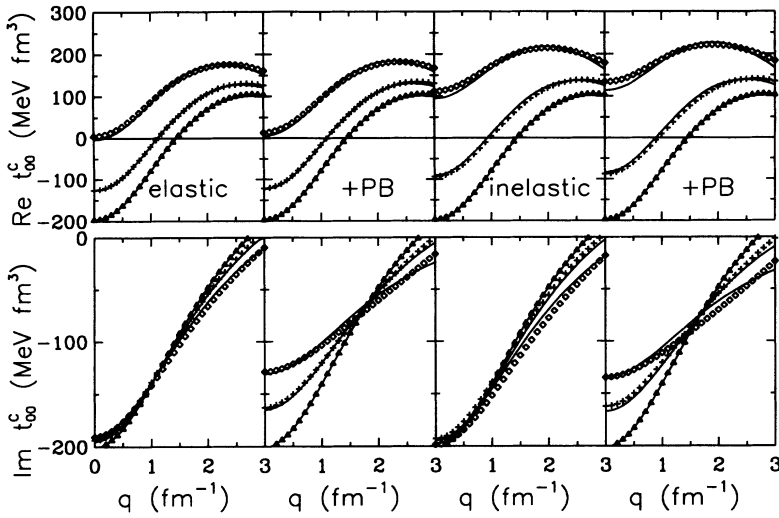


FIG. 1. Isoscalar spin-independent central components of the IA2 effective interaction at 200 MeV for $k_F = 0.0, 1.0,$ and 1.4 fm^{-1} are indicated by triangles, crosses, and diamonds, respectively. The top row shows the real parts and the bottom row the imaginary parts. The first column displays the elastic interaction without Pauli blocking, the second the elastic interaction with Pauli blocking, the third the inelastic interaction without Pauli blocking, and the fourth the inelastic interaction with Pauli blocking. The lines represent fits to the interactions based upon the parametrization of Eq. (3).

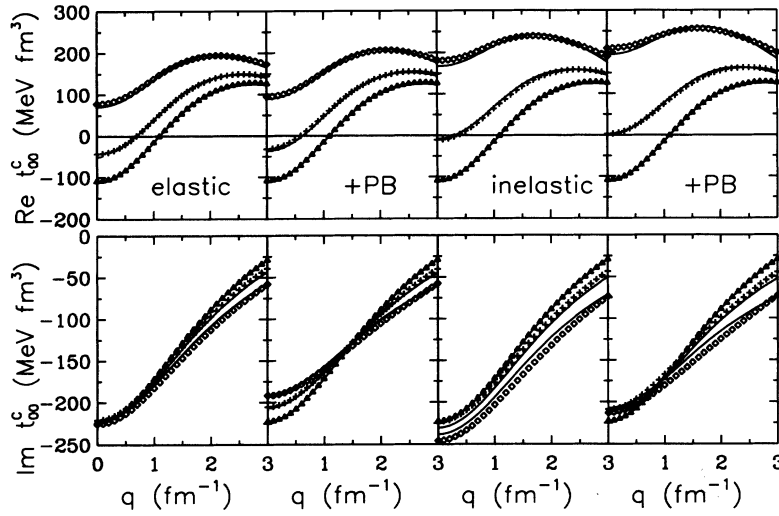


FIG. 2. Isoscalar spin-independent central components of the IA2 effective interaction at 318 MeV for $k_F = 0.0, 1.0,$ and 1.4 fm^{-1} are indicated by triangles, crosses, and diamonds, respectively. The top row shows the real parts and the bottom row the imaginary parts. The first column displays the elastic interaction without Pauli blocking, the second the elastic interaction with Pauli blocking, the third the inelastic interaction without Pauli blocking, and the fourth the inelastic interaction with Pauli blocking. The lines represent fits to the interactions based upon the parametrization of Eq. (3).

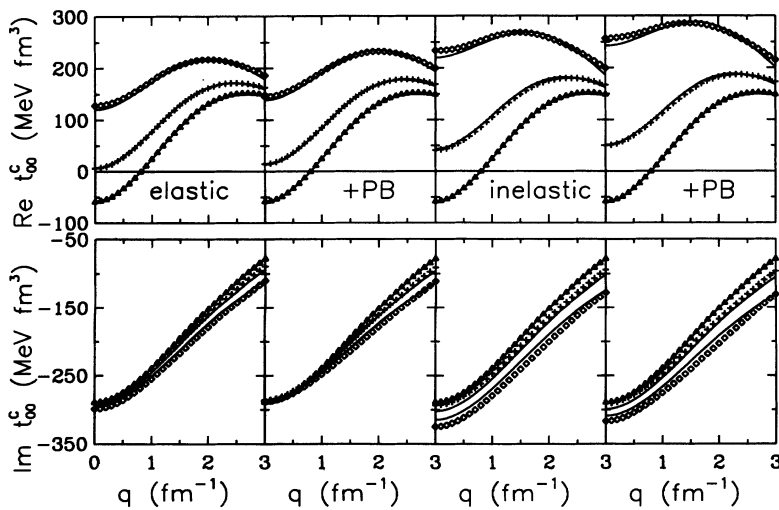


FIG. 3. Isoscalar spin-independent central components of the IA2 effective interaction at 500 MeV for $k_F = 0.0, 1.0,$ and 1.4 fm^{-1} are indicated by triangles, crosses, and diamonds, respectively. The top row shows the real parts and the bottom row the imaginary parts. The first column displays the elastic interaction without Pauli blocking, the second the elastic interaction with Pauli blocking, the third the inelastic interaction without Pauli blocking, and the fourth the inelastic interaction with Pauli blocking. The lines represent fits to the interactions based upon the parametrization of Eq. (3).

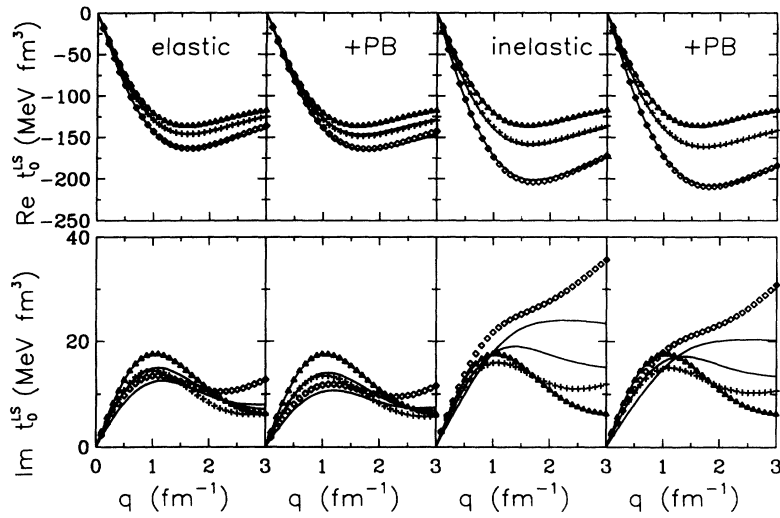


FIG. 4. Isoscalar spin-orbit components of the IA2 effective interaction at 200 MeV for $k_F = 0.0, 1.0,$ and 1.4 fm^{-1} are indicated by triangles, crosses, and diamonds, respectively. The top row shows the real parts and the bottom row the imaginary parts. The first column displays the elastic interaction without Pauli blocking, the second the elastic interaction with Pauli blocking, the third the inelastic interaction without Pauli blocking, and the fourth the inelastic interaction with Pauli blocking. The lines represent fits to the interactions based upon the parametrization of Eq. (3).

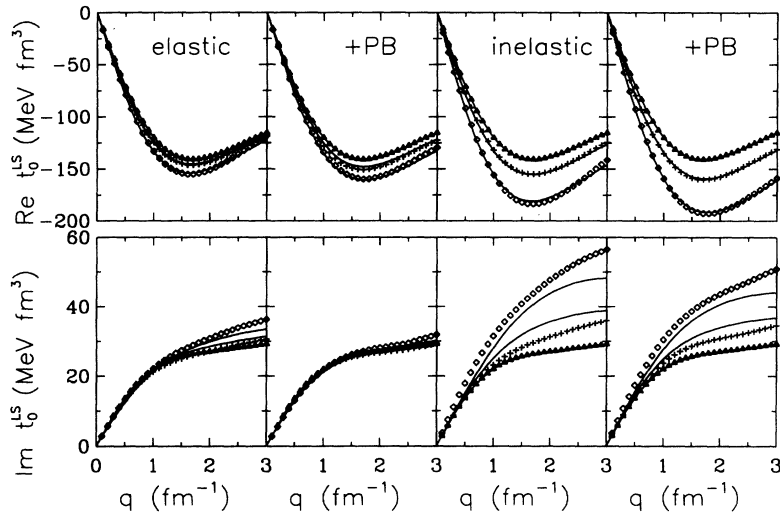


FIG. 5. Isoscalar spin-orbit components of the IA2 effective interaction at 318 MeV for $k_F = 0.0, 1.0,$ and 1.4 fm^{-1} are indicated by triangles, crosses, and diamonds, respectively. The top row shows the real parts and the bottom row the imaginary parts. The first column displays the elastic interaction without Pauli blocking, the second the elastic interaction with Pauli blocking, the third the inelastic interaction without Pauli blocking, and the fourth the inelastic interaction with Pauli blocking. The lines represent fits to the interactions based upon the parametrization of Eq. (3).

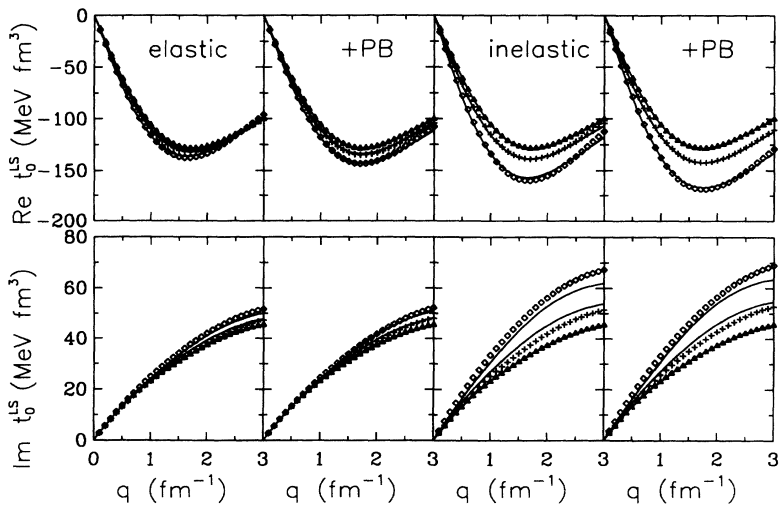


FIG. 6. Isoscalar spin-orbit components of the IA2 effective interaction at 500 MeV for $k_F = 0.0, 1.0,$ and 1.4 fm^{-1} are indicated by triangles, crosses, and diamonds, respectively. The top row shows the real parts and the bottom row the imaginary parts. The first column displays the elastic interaction without Pauli blocking, the second the elastic interaction with Pauli blocking, the third the inelastic interaction without Pauli blocking, and the fourth the inelastic interaction with Pauli blocking. The lines represent fits to the interactions based upon the parametrization of Eq. (3).

relationship between elastic and inelastic interactions remains the same as described at 200 MeV. The density dependence of the IA2 interaction at 318 MeV is similar to that of the empirical effective interaction for the real central component but is substantially less for the real spin-orbit component. Since these relationships are the opposite of those found at 200 MeV, the energy dependences of these two models are rather different.

The energy dependence of the imaginary central component is also very interesting. In the absence of Pauli blocking the damping coefficient is almost the same at both 200 and 318 MeV, but the short-range component (coefficient a_{21}) is almost twice as strong at 318 MeV and is significantly enhanced for inelastic scattering. Consequently, the strength of the imaginary central interaction for inelastic scattering is seen in Fig. 2 to increase with density for most of the q range. This effect, which is the opposite of Pauli blocking, was previously found when fitting an empirical effective interaction to data for inelastic scattering. In that analysis not only was the damping due to Pauli blocking absent, but a small enhancement of the absorptive interaction was found. Although it was speculated that pion production might be enhanced by off-shell effects at high density, perhaps the IA2 model provides a simpler explanation of this effect.

The effect of Pauli blocking upon elastic and inelastic interactions is also illustrated in Figs. 2 and 5. The damping of the imaginary central interaction is smaller at 318 MeV than at 200 MeV, but is still sufficient to mask the density-dependent enhancement of the interaction without Pauli blocking. Hence, at low q the elastic interaction retains the damping characteristics seen at lower energies. For the inelastic interaction, however, the short-range component is enhanced so there is little damping at low q and an appreciable enhancement at high q . Therefore, the q dependence of medium modifications of this component is considerably different from that assumed in previous analyses of the empirical effective interaction. It may be of interest to reanalyze the data using a form closer to the IA2 predictions.

3. $E_p = 500$ MeV

The isoscalar spin-independent central and isoscalar spin-orbit components of the IA2 effective interactions for 500 MeV are shown in Figs. 3 and 6, respectively. The density dependence continues to be independent of energy for Ret_{00}^C and to decline for Ret_{00}^{LS} . The density dependence of Ret_{00}^C is very similar to the empirical effective interaction, but is almost twice as strong as predicted by the nonrelativistic nuclear matter calculation of Ray. However, the density dependence of Ret_{00}^{LS} is now substantially less than for the empirical interaction.

The short-range component of the density dependence for $\text{Im}t_{00}^C$ continues to strengthen as the energy increases and is considerably enhanced for inelastic scattering. The damping of the imaginary central interaction is quite small at 500 MeV, but still reduces the density-dependent enhancement of the interaction without Pauli blocking. For the inelastic interaction, however, the short-range

component is strongly enhanced even after inclusion of Pauli blocking. Therefore, at 500 MeV the IA2 interaction resembles the empirical effective interaction much more closely than at lower energies. However, since the short-ranged component in the IA2 model of $\text{Im}t_{00}^C$ decreases more slowly with momentum transfer than assumed in the EEI model, it may be interesting to reanalyze the data with an interaction of this form.

III. ELASTIC SCATTERING

The Schrödinger equation with relativistic kinematics is customarily expressed in the form

$$(p^2 - k^2 + 2\mu U) \Psi = 0, \quad (6)$$

where k is the exact relativistic wave number in the NA frame and μ is the reduced total energy. The optical potential has the form

$$U(r) = U^Z(r) + U^C(r) + U^{LS}(r)\mathbf{L} \cdot \boldsymbol{\sigma}, \quad (7)$$

where U^Z is the Coulomb potential, U^C is the central potential, and $U^{LS} = \frac{1}{r} \frac{\partial F^{LS}}{\partial r}$ is the spin-orbit potential. In the folding model, the central and spin-orbit potentials become

$$U^C(r) = \frac{2}{\pi} \int dq q^2 j_0(qr) \eta t^C(q, \rho) \bar{\rho}(q), \quad (8)$$

$$F^{LS}(r) = \frac{2}{\pi} \int dq q^2 j_0(qr) \eta t'^{LS}(q, \rho) \bar{\rho}(q), \quad (9)$$

where

$$\bar{\rho}(q) = \int dr r^2 j_0(qr) \rho(r) \quad (10)$$

is the Fourier transform of the ground-state density ρ . Note that a sum over nucleon or isospin indices has been left implicit. For simplicity, the density dependence of the effective interaction is evaluated at the site of the projectile, but we find that other prescriptions give very similar results.

In nonrelativistic models, η is interpreted as the Jacobian between NN and NA frames [51] and is often called the Moller factor. However, since the nonrelativistic reduction of the IA2 model is performed in the NA frame and gives a wave equation of slightly different form, the Jacobian must be replaced by $\eta = \frac{E}{\mu}$, where $E^2 = k^2 + m^2$ is the projectile energy in the NA center-of-mass frame, to cast both models in the same form. Furthermore, since the IA2 model is relativistically covariant, the transformation between NN and NA frames is more complicated than the simple Moller factor used by nonrelativistic models.

To minimize uncertainties due to the nuclear density, the proton density was obtained by unfolding the nucleon charge form factor from the charge densities measured by electron scattering and tabulated in Refs. [52–54]. For self-conjugate targets and relatively small momentum transfers, charge symmetry ensures that the neutron and proton densities are very nearly equal. We find

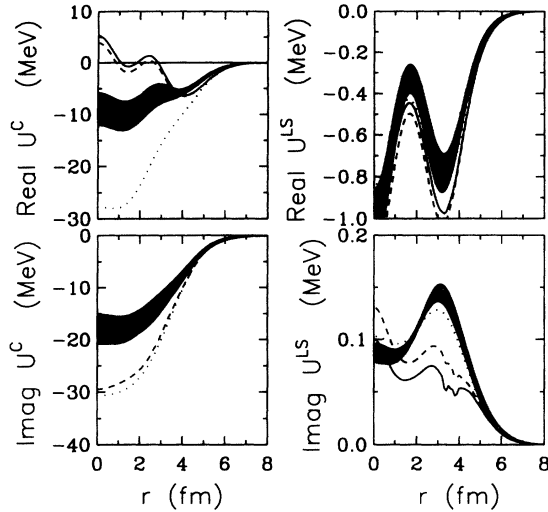


FIG. 7. Optical potentials for ^{40}Ca at 200 MeV. The bands represent the spread among several empirical effective interactions fitted to data for elastic and inelastic scattering for ^{16}O and/or ^{40}Ca . The dotted lines omit density dependence, the dashed lines include relativistic corrections, and the solid lines include Pauli blocking corrections based upon the IA2 model.

that inclusion of theoretical estimates of the differences between neutron and proton densities, as calculated by Dechargé and Gogny [55,56], has little effect upon the results. The differences between scalar and vector densities are included implicitly by the IA2 effective interaction [28].

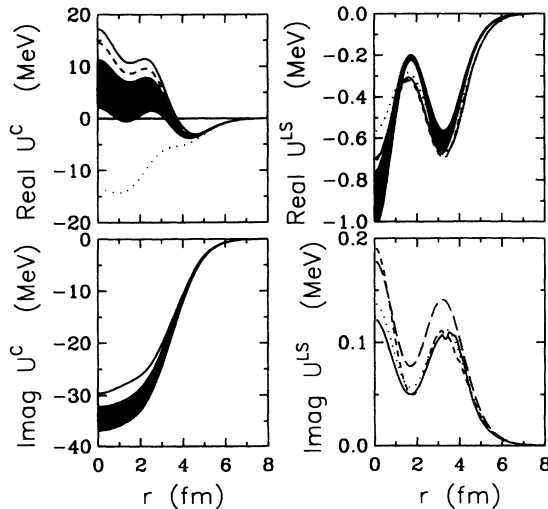


FIG. 8. Optical potentials for ^{40}Ca at 318 MeV. The bands represent the spread among several empirical effective interactions fitted to data for elastic and inelastic scattering for ^{16}O and/or ^{40}Ca . The long-dashed curve for $\text{Im}U^{LS}$ was used with the EEI model. The dotted lines omit density dependence, the dashed lines include relativistic corrections, and the solid lines include Pauli blocking corrections based upon the IA2 model.

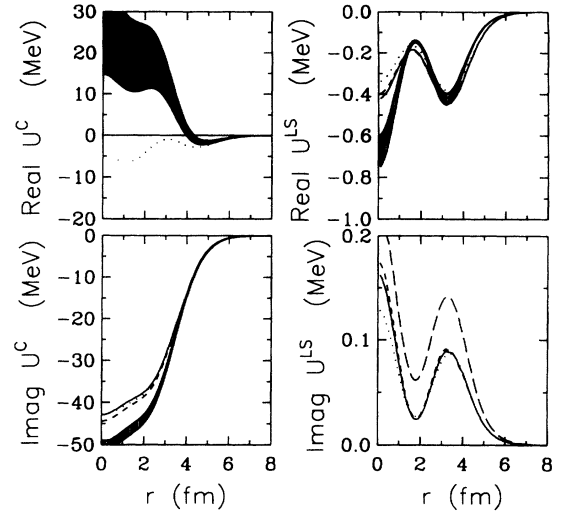


FIG. 9. Optical potentials for ^{40}Ca at 500 MeV. The bands represent the spread among several empirical effective interactions fitted to data for elastic and inelastic scattering for ^{16}O and/or ^{40}Ca . The long-dashed curve for $\text{Im}U^{LS}$ was used with the EEI model. The dotted lines omit density dependence, the dashed lines include relativistic corrections, and the solid lines include Pauli blocking corrections based upon the IA2 model.

The optical potentials that result from several variations of the IA2 effective interaction are compared with those of the empirical effective interaction at 200, 318, and 500 MeV in Figs. 7–9. The bands represent the spread among potentials corresponding to various fits of the effective interaction to data for ^{16}O and ^{40}Ca and provide an estimate of the uncertainty in the optical potentials. The *m* spinor potential based upon free (undistorted) Dirac spinors is shown by dotted curves. The potential obtained by using distorted Dirac spinors is shown by dashed curves. The principal relativistic effect is to allow for modification of the lower components of the Dirac spinors in the nuclear medium. The net result is a short-ranged repulsive interaction contributing primarily to the real central potential. The complicated radial shapes of the real central potentials result from the folding of a nonuniform density with a strongly density-dependent interaction and are similar to the findings of nonrelativistic models of the effective interaction. The solid curves also include Pauli blocking, for which the principal effect is seen to be damping of the absorptive potential.

A. $E_p = 200$ MeV

Fig. 7 shows that the repulsive contribution to the IA2 central interaction at 200 MeV is considerably stronger than predicted by nonrelativistic models and is stronger than that of the empirical effective interaction. In addition, relativistic effects significantly enhance the real spin-orbit potential. Finally, the damping of the absorp-

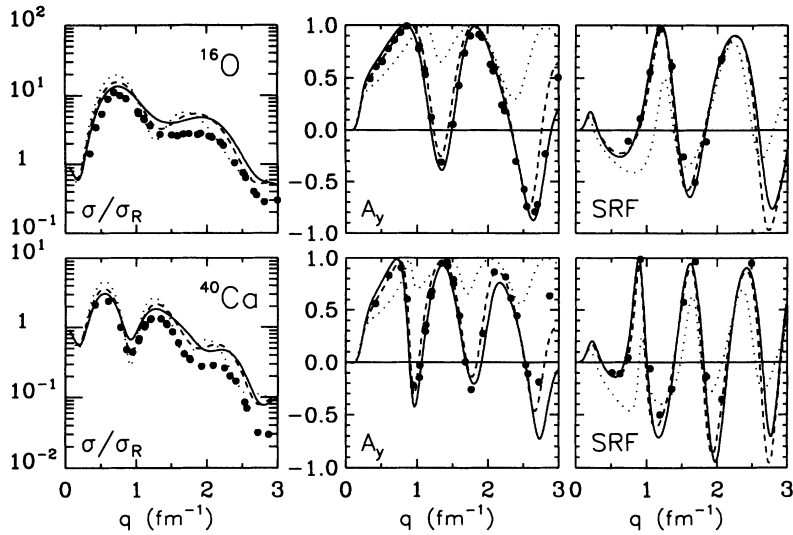


FIG. 10. Elastic scattering calculations based upon the IA2 effective interaction are compared with data for ^{16}O and ^{40}Ca at 200 MeV. The dotted lines omit density dependence, the dashed lines include relativistic corrections, and the solid lines include Pauli blocking corrections based upon the IA2 model also.

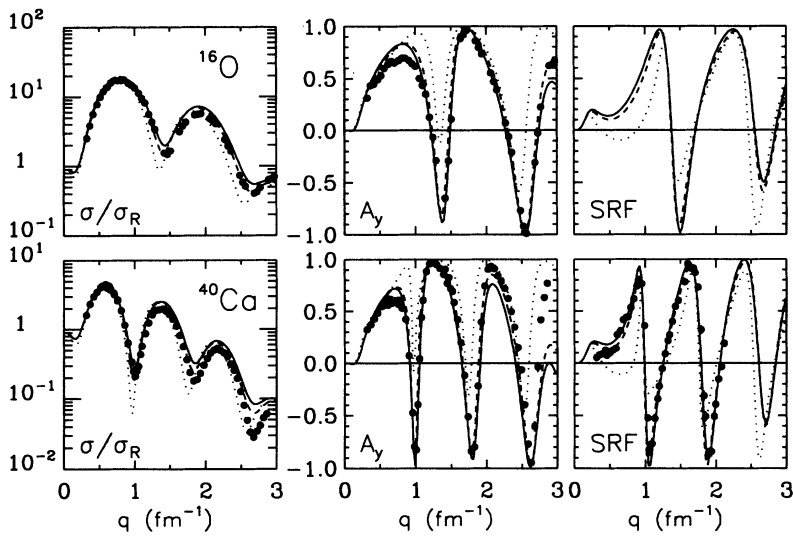


FIG. 11. Elastic scattering calculations based upon the IA2 effective interaction are compared with data for ^{16}O and ^{40}Ca at 318 MeV. The dotted lines omit density dependence, the dashed lines include relativistic corrections, and the solid lines include Pauli blocking corrections based upon the IA2 model also.

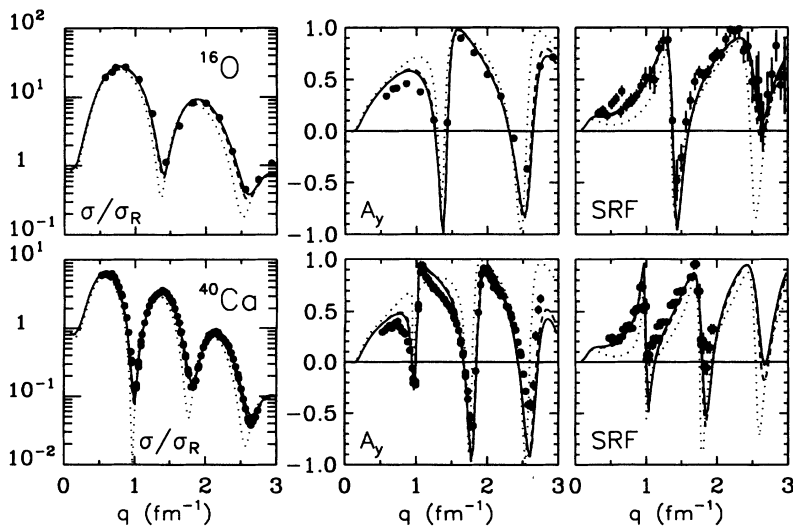


FIG. 12. Elastic scattering calculations based upon the IA2 effective interaction are compared with data for ^{16}O and ^{40}Ca at 500 MeV. The dotted lines omit density dependence, the dashed lines include relativistic corrections, and the solid lines include Pauli blocking corrections based upon the IA2 model also.

tive potential due to Pauli blocking is consistent with that found in the empirical interaction.

Selected elastic scattering results are shown in Fig. 10. The data were obtained from Refs. [36] and [57]. The relativistic repulsion gives remarkable improvements to calculations of the analyzing power (A_y) and spin rotation function (SRF). For the analyzing power, in particular, the density-dependent repulsion is responsible for sharp oscillations which would otherwise be absent from the impulse approximation. This contribution also reduces the forward cross section, but that effect alone is not strong enough to provide good agreement with the data. When Pauli blocking is included also the forward cross section is reduced further, but the elastic cross section at larger momentum transfer remains substantially above the data. These observations are common to both ^{16}O and ^{40}Ca . Note that we plot the ratio with respect to the point-Coulomb (Rutherford) cross section to enhance the visibility of such details.

Evidently the density dependence of the real central and spin-orbit components of the IA2 interaction is stronger at 200 MeV than required by the data. Although these effects partly compensate each other in the analyzing power, they both deleteriously reinforce the cross section calculation at high q . The nonrelativistic nuclear matter theories predict less density dependence in these components and are more successful at this energy in describing the elastic cross section and analyzing power data simultaneously.

B. $E_p = 318$ MeV

Optical potentials from the IA2 model are compared with those of the empirical effective interaction at 318 MeV in Fig. 8. At this energy the repulsive relativistic contribution to the real central potential is similar to the phenomenological density dependence, giving $\text{Re}U^C$ just above the upper edge of the empirical band. The relativistic effect upon the real spin-orbit potential is smaller at 318 MeV than at 200 MeV but produces a potential similar to the empirical potential. However, since $\text{Re}t_0^{LS}$ must be suppressed at low density for the EEI to give good fits to the data, $\text{Re}U^{LS}$ is significantly smaller at the surface for the EEI model than for the IA2 model. Perhaps the most significant difference between the IA2 and empirical potentials is found in the imaginary central component, for which the relativistic effects are negligible, but Pauli blocking significantly damps the absorptive potential. Thus, the IA2 model yields a result similar to the nonrelativistic G -matrix models for this component, whereas the empirical absorption is enhanced with respect to the free interaction. Therefore, the enhanced absorption in the empirical effective interaction, which is opposite the effect expected from Pauli blocking, is not explained by the IA2 model for energies near 300 MeV.

Elastic scattering calculations are compared with data from Refs. [37,38,58] in Fig. 11. The relativistic repulsion provides a dramatic improvement in the analyzing power and spin rotation calculations, with markedly sharper oscillations due to the repulsive contribution to the central

interaction. However, the analyzing power calculation for $q \approx 0.7 \text{ fm}^{-1}$ remains somewhat too large, whereas the empirical effective interaction overcompensates slightly [37,38]. For the elastic cross section, on the other hand, the relativistic contribution shifts the angular distribution to larger momentum transfer. Pauli blocking reinforces this effect, giving elastic cross sections that are too strong at high q . This effect is similar to but less pronounced than at 200 MeV. The fact that the empirical effective interaction fitted to inelastic scattering from ^{16}O consistently fits the cross section, analyzing power, and spin rotation data for elastic scattering from ^{40}Ca suggests that the differences between the two models of the effective interaction are more than just an artifact of the phenomenological parametrization and that the enhancement of the imaginary central interaction is required.

C. $E_p = 500$ MeV

Optical potentials for $p+^{40}\text{Ca}$ at 500 MeV from the IA2 and EEI models are compared in Fig. 9. The width of the uncertainty band for $\text{Re}U^C$ in the interior grows with energy because increasing absorption reduces penetrability and the strength of $\text{Re}U^C$ is relatively small compared with $\text{Im}U^C$ in this energy regime. The relativistic repulsion in the real central potential is consistent with the empirical fit to the data, lying nearly in the center of the band. The most significant difference between the EEI and IA2 models is found in $\text{Im}U^C$, for which the IA2 and m -spinor predictions are almost identical but for which the EEI potential is enhanced with respect to the impulse approximation. Pauli blocking is still strong enough at this energy to nullify the low- q enhancement of $\text{Im}t_0^C$ in the elastic interaction. We again find that the scaling of $\text{Re}t_0^{LS}$ at low density required by the EEI analysis results in a reduction of $\text{Re}U^{LS}$ at the surface relative to the IA2 model.

Elastic scattering calculations are compared with the data in Fig. 12. The data for ^{16}O are from Ref. [39] and for ^{40}Ca from Ref. [59]. The relativistic repulsion shifts the cross section angular distribution to larger momentum transfer and improves the agreement with the data. Similarly, the angular distributions for the analyzing power and spin rotation function are improved by the relativistic contribution. The effect of Pauli blocking upon the elastic scattering calculations for 500 MeV is very small. The agreement with the data is essentially the same as obtained by Ottenstein *et al.* [19] with the full IA2 model. However, the analyzing power for low q remains too strong and the oscillations are too sharp for both A_y and the spin-rotation function. Better descriptions for these observables are obtained with the EEI model [39], albeit with fitting parameters.

IV. NORMAL-PARITY ISOSCALAR TRANSITIONS

For the strong normal-parity excitations considered herein, the transverse form factors observed in electron scattering measurements are small, indicating that the

relevant spin and current densities are negligible. Furthermore, we assume that other types of spin and current densities which could affect nucleon scattering but which are absent in electroexcitation are also negligible [60,61]. The scattering potential $U(\mathbf{r})$ which excites normal-parity excitations then reduces to the form

$$U(\mathbf{r}) = U^Z(\mathbf{r}) + U^C(\mathbf{r}) + \nabla F^{LS}(\mathbf{r}) \otimes \frac{1}{i} \nabla \cdot \boldsymbol{\sigma}, \quad (11)$$

where the potentials can be expanded in multipoles of the form

$$U^C(\mathbf{r}) = \sum_J U_J^C(r) \cdot Y_J(\hat{r}), \quad (12)$$

$$F^{LS}(\mathbf{r}) = \sum_J F_J^{LS}(r) \cdot Y_J(\hat{r}), \quad (13)$$

with

$$U_J^C(r) = \frac{2}{\pi} \int dq q^2 j_J(qr) \eta t^C(q, \rho) \bar{\rho}_J(q), \quad (14)$$

$$F_J^{LS}(r) = \frac{2}{\pi} \int dq q^2 j_J(qr) \eta t'^{LS}(q, \rho) \bar{\rho}_J(q), \quad (15)$$

where $\bar{\rho}_J(q)$ is the matter transition density for multipolarity J . A sum over isospin or nucleon labels remains implicit. In nonrelativistic models, the effective interaction applicable to inelastic scattering is usually related to the effective interaction for elastic scattering in nuclear matter by means of the Cheon rearrangement relation

$$t^{\text{inelastic}}(q, \rho) = (1 + \partial/\partial\rho) t^{\text{elastic}}(q, \rho). \quad (16)$$

However, the IA2 model provides a method for calculating the effective interaction for inelastic scattering directly without recourse to the Cheon prescription.

To minimize uncertainties due to nuclear structure, the proton transition densities were constructed by unfolding the nucleon charge form factor from transition charge densities measured by electron scattering. We assume that the neutron and proton transition densities for self-conjugate targets are essentially identical for momentum transfers below 3 fm^{-1} . Transition densities were obtained from Ref. [62] for ^{16}O and from Ref. [63] for ^{40}Ca .

States whose transition densities contain a strong interior lobe provide optimum sensitivity to the high-density properties of the effective interaction. Examples of this type include the lowest 1^- state of ^{16}O and the second and third 3^- states of ^{40}Ca . States with surface-peaked transition densities, typically the lowest collective states of each multipolarity (with $J > 1$), provide optimum sensitivity to the low-density properties of the effective interaction. Unlike elastic scattering, which is sensitive to an average over density, comparisons between inelastic scattering using interior and surface transition densities provide considerable differential sensitivity to the density dependence of the effective interaction. This differential sensitivity is exploited by phenomenological analyses of the effective interaction.

Calculations of differential cross sections and analyzing powers for inelastic scattering of 200, 318, and 500

MeV protons by ^{16}O are compared with data for selected transitions in Figs. 13–15. Similar comparisons for ^{40}Ca are shown in Figs. 16–18. Finally depolarization data for 500 MeV protons are compared with IA2 calculations in Figs. 19 and 20. These comparisons are discussed below for each energy in turn. The dotted curves are based upon the free interaction, the long-dashed curves include relativistic corrections, and the solid curves include Pauli blocking also. For these calculations both the distorting potentials and the scattering potentials were computed from the same effective interactions, except that the additional density dependence of the inelastic interaction was included in the scattering potential. To illustrate the importance of enhanced inelastic density dependence, additional calculations which employ the elastic IA2 interaction for inelastic scattering, without Pauli blocking or rearrangement contributions, are shown as short-dashed curves. Thus, the rearrangement effect is seen in the difference between the short-dashed and long-dashed curves and the effect of Pauli blocking in the difference between long-dashed and solid curves.

A. $E_p = 200 \text{ MeV}$

Selected inelastic scattering calculations are shown in Figs. 13 and 16. The data were obtained from Ref. [36]. For analyzing powers the density-dependent repulsion in Ret_{00}^C provides a marked improvement over the free interaction. The density dependence of the interaction has a modest effect upon the cross section calculation at low momentum transfer, but for larger momentum transfer the relativistic repulsion, rearrangement, and Pauli blocking all increase the cross section significantly. For surface excitations, such as the 3_1^- states of both ^{16}O and ^{40}Ca , the IA2 cross section calculations are too large and do not describe the angular distributions particularly well. For states whose transition densities have strong interior lobes, such as the 1_1^- state of ^{16}O or the 3_2^- state of ^{40}Ca , the IA2 model is a little more successful at low q but the density dependence at high q remains too strong. Similar characteristics have been observed in calculations for many other states, but space limitations preclude their presentation. Furthermore, these features of the IA2 calculations are also observed in elastic scattering and hence represent general properties of the model. These features are described more accurately by some of the nonrelativistic effective interactions, such as the PH or LR models, with smaller density dependence in Ret_{00}^C and Ret_0^{LS} . Also note that increasing the density dependence of the inelastic $\text{Im}t_{00}^C$ according to the Cheon prescription could improve the accuracy of the IA2 interactions, but that effect appears to be missing from the IA2 model.

The empirical effective interaction achieves a much better fit to the inelastic cross section data using less density dependence, in part by reducing the interaction strengths at zero density. In Ref. [34] it was suggested that the density dependence appropriate to a finite nucleus should be larger at low density and weaker at high density than for infinite nuclear matter with correspond-

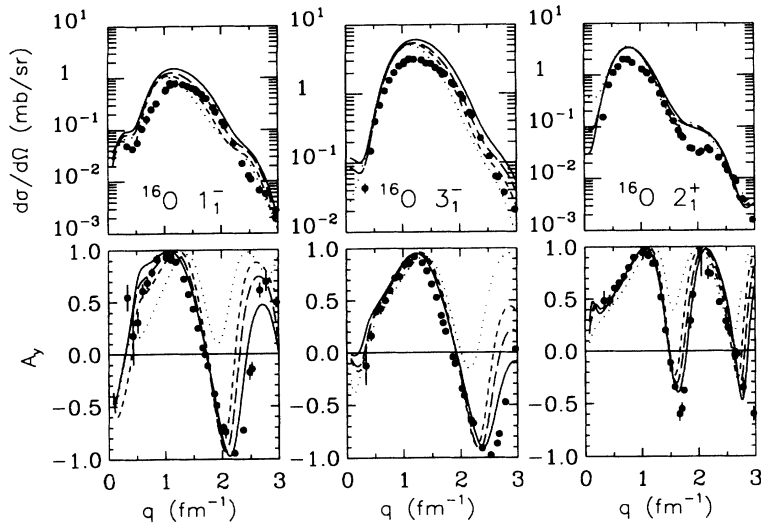


FIG. 13. Inelastic scattering calculations based upon the IA2 effective interaction are compared with data for selected states of ^{16}O at 200 MeV. The dotted lines omit density dependence, the short-dashed lines use the elastic interaction without Pauli blocking, the long-dashed lines use the inelastic interaction without Pauli blocking, and the solid lines use the inelastic interaction and include Pauli blocking.

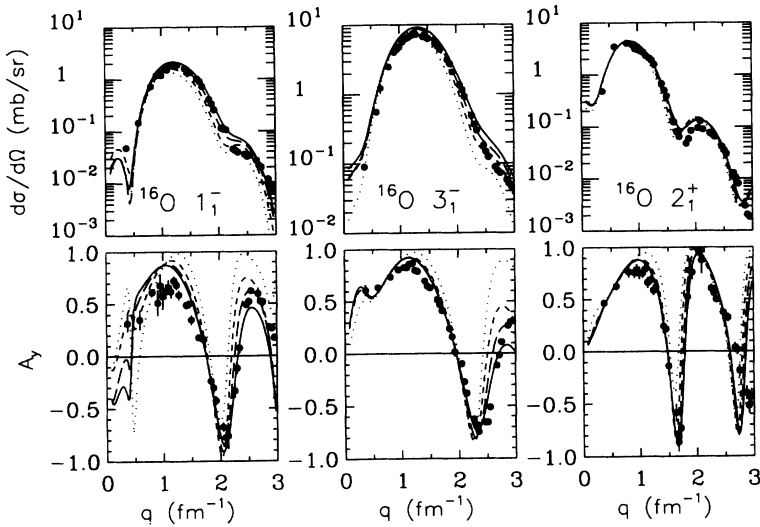


FIG. 14. Inelastic scattering calculations based upon the IA2 effective interaction are compared with data for selected states of ^{16}O at 318 MeV. The dotted lines omit density dependence, the short-dashed lines use the elastic interaction without Pauli blocking, the long-dashed lines use the inelastic interaction without Pauli blocking, and the solid lines use the inelastic interaction and include Pauli blocking.

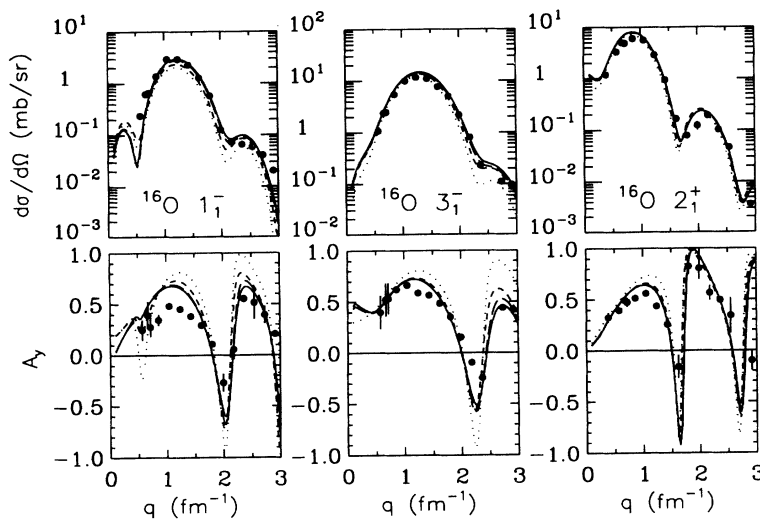


FIG. 15. Inelastic scattering calculations based upon the IA2 effective interaction are compared with data for selected states of ^{16}O at 500 MeV. The dotted lines omit density dependence, the short-dashed lines use the elastic interaction without Pauli blocking, the long-dashed lines use the inelastic interaction without Pauli blocking, and the solid lines use the inelastic interaction and include Pauli blocking.

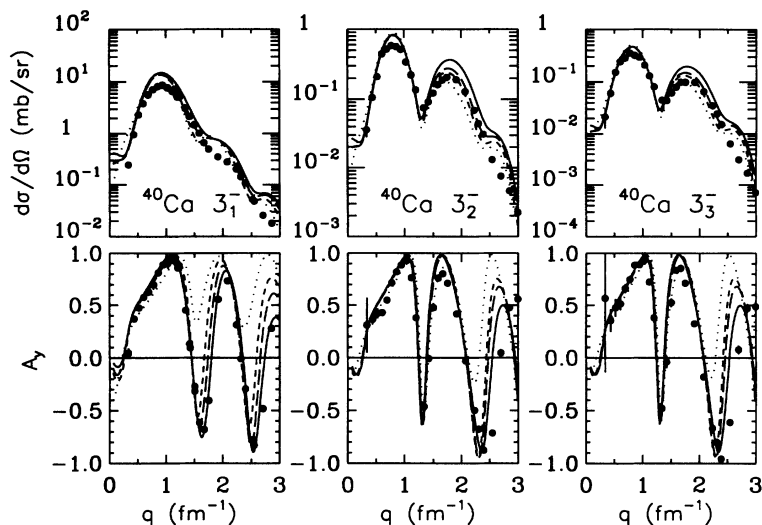


FIG. 16. Inelastic scattering calculations based upon the IA2 effective interaction are compared with data for selected states of ^{40}Ca at 200 MeV. The dotted lines omit density dependence, the short-dashed lines use the elastic interaction without Pauli blocking, the long-dashed lines use the inelastic interaction without Pauli blocking, and the solid lines use the inelastic interaction and include Pauli blocking.

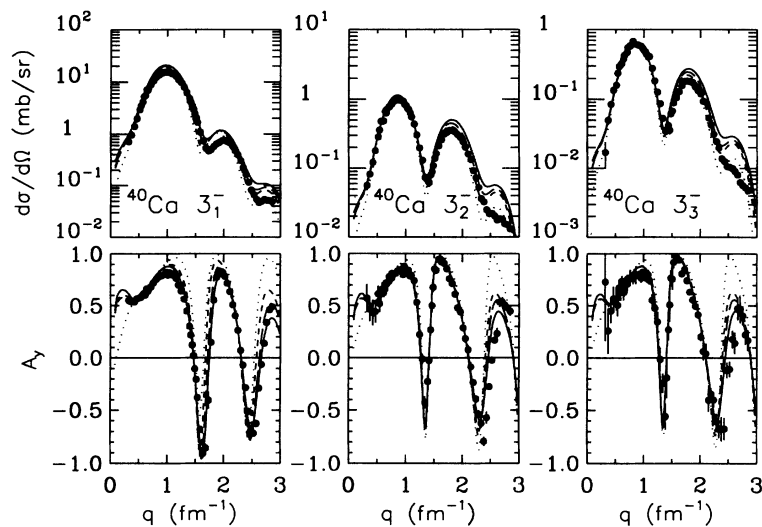


FIG. 17. Inelastic scattering calculations based upon the IA2 effective interaction are compared with data for selected states of ^{40}Ca at 318 MeV. The dotted lines omit density dependence, the short-dashed lines use the elastic interaction without Pauli blocking, the long-dashed lines use the inelastic interaction without Pauli blocking, and the solid lines use the inelastic interaction and include Pauli blocking.

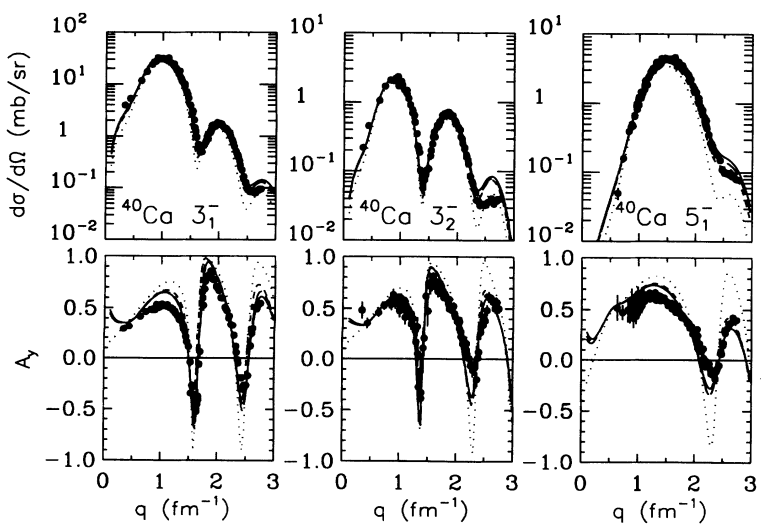


FIG. 18. Inelastic scattering calculations based upon the IA2 effective interaction are compared with data for selected states of ^{40}Ca at 500 MeV. The dotted lines omit density dependence, the short-dashed lines use the elastic interaction without Pauli blocking, the long-dashed lines use the inelastic interaction without Pauli blocking, and the solid lines use the inelastic interaction and include Pauli blocking.

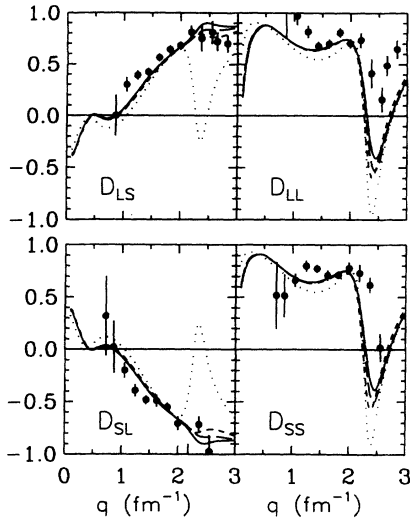


FIG. 19. Calculations based upon the IA2 effective interaction of depolarization observables for the lowest 3^- state of ^{16}O are compared with data for 500 MeV protons. The dotted lines omit density dependence, the short-dashed lines use the elastic interaction without Pauli blocking, the long-dashed lines use the inelastic interaction without Pauli blocking, and the solid lines use the inelastic interaction and include Pauli blocking.

ing densities, as per the LDA. It was found that it was not possible to fit the data using empirical models whose density dependence resembles that of the IA2 unless the zero-density limit was adjusted also. Furthermore, in order to obtain a consistent fit to the elastic and inelastic scattering data simultaneously, it was found necessary to

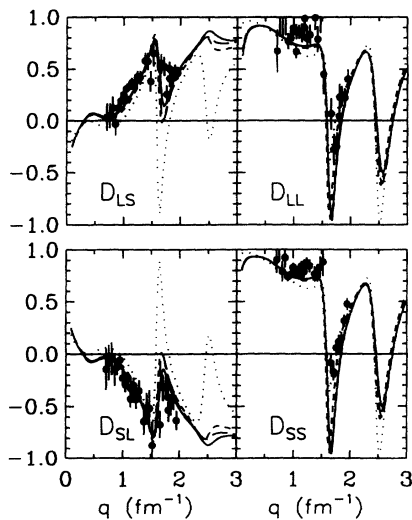


FIG. 20. Calculations based upon the IA2 effective interaction of depolarization observables for the lowest 3^- state of ^{40}Ca are compared with data for 500 MeV protons. The dotted lines omit density dependence, the short-dashed lines use the elastic interaction without Pauli blocking, the long-dashed lines use the inelastic interaction without Pauli blocking, and the solid lines use the inelastic interaction and include Pauli blocking.

include a rearrangement relationship of the Cheon type between the elastic and inelastic interactions.

B. $E_p = 318$ MeV

Inelastic scattering calculations are compared with data from Refs. [37] and [38] in Figs. 14 and 17. The relativistic repulsion again provides a good description of the analyzing power data, although there remains some tendency for the calculations to be too strong preceding the first diffraction dip. Qualitatively better agreement with the inelastic cross section data is obtained at 318 MeV than at 200 MeV with the IA2 interaction. However, the inelastic cross section predictions are too strong for large momentum transfer, particularly when rearrangement and/or Pauli blocking is included. These effects are qualitatively similar to but somewhat smaller than those seen at 200 MeV and are consistent with the outward shift of the elastic angular distribution.

C. $E_p = 500$ MeV

Calculations for selected transitions are compared with the data for 500 MeV protons in Figs. 15 and 18. The data were obtained from Refs. [39,64–66]. The quality of the agreement with data is quite similar for both elastic and inelastic scattering at this energy. The density dependence of the effective interaction shifts the cross section angular distributions to larger momentum transfer and damps the oscillations in the analyzing power calculations. However, the oscillations in the analyzing power low momentum transfer remain too strong with the IA2 interaction and are described better with the EEI model. The effect of medium modifications upon the calculation of depolarization observables, illustrated in Figs. 19 and 20 for the 3^- states of ^{16}O and ^{40}Ca , is particularly striking for $q \approx 2.5 \text{ fm}^{-1}$, where the density-independent interaction predicts sharp oscillations in D_{LS} and D_{SL} which have incorrect signs. These features of the data are described very well by the IA2 effective interaction, although for ^{40}Ca the oscillations near 2 fm^{-1} appear to remain too sharp.

It is interesting to note that medium modifications of the effective interaction affect cross section calculations for states with strong interior transition densities quite differently at 500 MeV compared with energies below 200 MeV. For low projectile energies, the impulse approximation for such transitions predicts cross sections for momentum transfer near and below the peak of the angular distribution that are several times stronger than the data. In nonrelativistic models, Pauli blocking corrections serve to reduce low- q and enhance high- q cross sections and thereby improve the accuracy of the angular distributions for such transitions. However, beginning near 300 MeV and increasing at 500 MeV, the peak cross sections for interior transitions are smaller than the data when computed with density-independent interactions. This effect is not reproduced well by nonrelativistic nuclear matter models, but is fitted in the empirical effective interaction

using an $\text{Im}t_{00}^C$ component that increases with density, contrary to expectations based upon Pauli blocking. As illustrated by the 1_1^- state of ^{16}O , this effect is described by the IA2 model in much the same manner. The rearrangement effect and Pauli blocking both act in the same manner and the net density dependence dramatically improves the agreement with the data, particularly for spin observables and for cross sections to states with interior transition densities.

V. DISCUSSION

Many of the features of the IA2 effective interaction for isoscalar normal parity transitions are similar to those of nonrelativistic models, but there are also important differences. The dominant effect of distortion of Dirac spinors is a strong repulsive contribution to the real central interaction that is in good agreement with empirical findings near 500 MeV, but which is much stronger at low energies than predicted by any of the nonrelativistic theories or fitted to data. The dominant effect of Pauli blocking is damping of absorption similar to that of the Clementel and Villi model. This effect decreases with energy and is similar to that in nonrelativistic theories. The density dependence of the real parts of both the central and spin-orbit interactions for inelastic scattering is approximately twice as strong as for elastic scattering, as predicted by the self-consistency argument of Cheon *et al.* [30,31], but there is little difference between the damping of the elastic and inelastic interactions. On the other hand, there is a significant short-range contribution to the imaginary-central component of the IA2 interaction whose density dependence is enhanced for inelastic scattering. Although this effect improves the agreement with the inelastic EEI, the enhanced absorption found with EEI fits to the data for $E_p > 300$ MeV remains unexplained by the IA2 model. Finally, the modifications of the low-density interactions required by the phenomenological analyses, particularly for low energies, have not yet been explained satisfactorily, but are probably due to finite-nucleus corrections to the local density approximation.

The parameters representing the density dependence of the central interaction for several models are compared with the empirical effective interaction in Fig. 21. No attempt to impose a smooth energy dependence upon the EEI analyses has yet been made. Also, note that there may exist correlations between these density-dependent parameters and the density-independent scale factors, which are not shown, which could affect the energy dependencies and the comparison between IA2 and EEI parameters to some degree. For example, the S_3 and b_3 parameters tend to be highly correlated, which probably contributes to the fluctuations in the fitted values of b_3 , but constraining the spin-orbit scale factor S_3 to unity adversely affects the quality of the fits to data, particularly for low energies. The parameters quoted for the DP1 model of Hama *et al.* [10] were obtained in Ref. [29] by fitting the parameters of Eqs. (4a)–(4c) directly to the Schrödinger equivalent optical potentials assuming

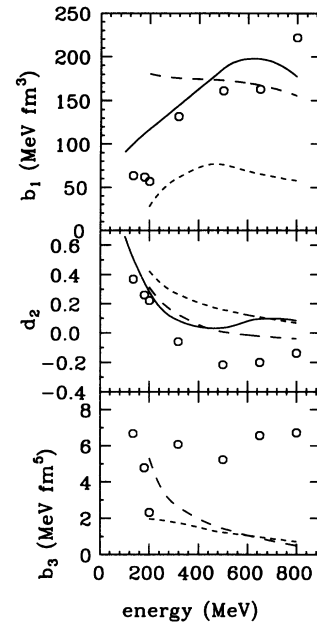


FIG. 21. Comparison between data for the empirical effective interaction (symbols) and the DP1 (solid), IA2 (long dashes), and LR (short dashes) models.

the free interaction could be adequately represented for each energy by the FL t matrix. Hence, the solid lines attribute the differences between global Dirac optical potentials and the nonrelativistic impulse approximation to medium modifications of the effective interaction. A similar analysis of IA2 optical potentials was performed also but is not shown because Pauli blocking was not included at that time. Instead, we plot the elastic IA2 interaction with Pauli blocking as represented in Table II. It is clear that the energy dependence of the DP1 model is closer to the EEI results than the IA2. Since the DP1 model is a relativistic phenomenology, it implicitly includes both relativistic density dependence and conventional medium modifications due to Pauli blocking and dispersion. Although the IA2 model includes the relativistic density dependence and some of the effects of Pauli blocking, it appears not to be sufficiently complete to describe the energy dependence of the effective interaction.

An important difference between the relativistic and nonrelativistic impulse approximations may be found in the comparison between the interactions at zero density. As shown in Fig. 22, the $\text{Re}t_{00}^C$ component of the IA2 effective interaction for $p+^{40}\text{Ca}$ at 500 MeV is significantly stronger for $q > 2 \text{ fm}^{-1}$ than the Franey-Love t matrix. To simplify this comparison, the Moller factor is omitted from the FL t matrix and divided out of the IA2 t matrix in Fig. 22. That this difference is not due to the nucleon-nucleon (NN) scattering amplitudes is illustrated in Fig. 23, which compares the corresponding amplitudes in the NN c.m. frame. The small residual differences between the NN amplitudes can be attributed to changes in the phase-shift fits between the times of the two analyses and to differences in fitting procedures. The much larger difference in the two models of the nucleon-nucleus (NA)

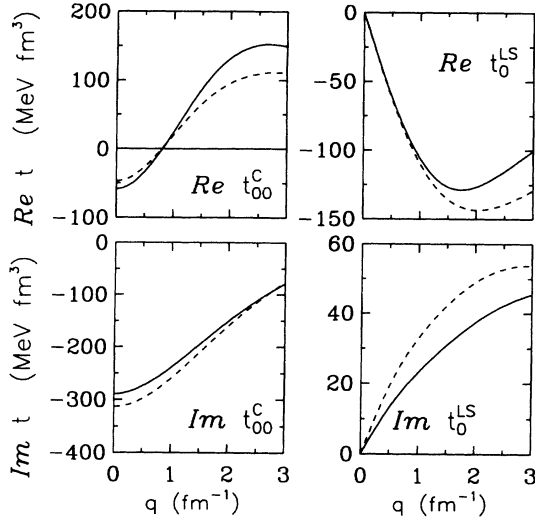


FIG. 22. Comparison between relativistic IA2 (solid) and nonrelativistic FL (dashed) nucleon-nucleus t matrices at 500 MeV for $k_F = 0$.

t matrix is due primarily to the transformation procedures. The Franey-Love prescription employs a static approximation for exchange and adjusts the t matrix by a simple Moller factor. The IA2 model employs invariant amplitudes to evaluate the nucleon-nucleus t matrix using optimal factorization in the Breit frame. At $q = 0$ this procedure reduces to a Moller factor, but at larger momentum transfer the struck particle is assigned momentum $-\mathbf{q}/2$ in the initial state and $+\mathbf{q}/2$ in the final state. Hence the on-shell amplitudes are evaluated for momenta which correspond to a higher effective energy. The stronger repulsion in the IA2 interaction occurs primarily in the direct amplitude and is relatively insensitive to the treatment of exchange.

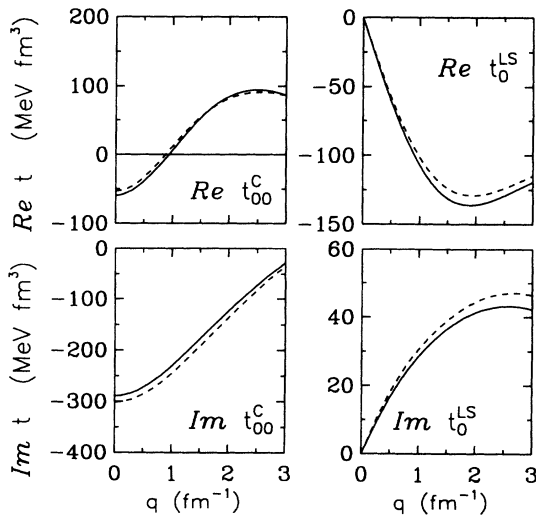


FIG. 23. Comparison between IA2 (solid) and FL (dashed) nucleon-nucleon t matrices at 500 MeV.

The effect of Breit-frame kinematics can be understood most simply in the σ - ω model, for which the central component becomes

$$\frac{1}{\eta} t_{00}^{C \text{ Breit}} = \frac{m^2}{E_c^2} \left(s(q) + \frac{E_{\text{Breit}}}{m} v(q) \right) + \delta t^{\text{Breit}} \quad (17)$$

in the Breit frame, compared with

$$t_{00}^{C \text{ c.m.}} = \frac{m^2}{E_c^2} \left(s(q) + \frac{E_L}{m} v(q) \right) + \delta t^{\text{c.m.}} \quad (18)$$

in the center of mass frame, where

$$s(q) = \frac{-g_\sigma^2}{q^2 + m_\sigma^2}$$

is the invariant amplitude for scalar meson exchange (attractive) and

$$v(q) = \frac{g_\omega^2}{q^2 + m_\omega^2}$$

is the invariant amplitude for vector meson exchange (repulsive). The factor E_{Breit}/m arises from the momenta in Dirac spinors when matrix elements of the $\gamma_1 \cdot \gamma_2$ coupling of the vector meson are evaluated in the Breit frame kinematics, whereas one obtains the factor E_L/m when on-shell spinors are used in the NN c.m. frame. The remaining terms δt^{Breit} and $\delta t^{\text{c.m.}}$ are very nearly equal and thus they do not affect the difference between $t_{00}^{C \text{ Breit}}$ and $t_{00}^{C \text{ c.m.}}$. The effective energy E_{Breit} for Breit-frame kinematics is related to the laboratory energy E_L by

$$E_{\text{Breit}} \approx E_L + \frac{\mathbf{q}^2}{4m} \left(1 + \frac{E_L}{2m} \right).$$

Since real parts of the scalar and vector interactions are both large and are of opposite signs, this kinematic effect upon the scattering amplitude is important, particularly at low energy and large momentum transfer. It explains the enhancement of $t_{00}^{C \text{ Breit}}$ seen in Fig. 22.

Although the $k_F \rightarrow 0$ limit of the IA2 interaction has been interpreted as a free or zero-density interaction, the use of Breit frame kinematics results in a significant difference from the on-shell interaction at high q . The reason is that an off-shell extrapolation of the t matrix is required for $q > 0$ and it is precisely this extrapolation which leads to the appearance of E_{Breit} in Eq. (17) as opposed to E_L in Eq. (18). The off-shell extrapolation is traceable to the optimal factorization, which is being used to approximate the full-folding integral in the impulse approximation. We note that the off-shell extrapolation which is obtained by use of the Lorentz invariant amplitudes is quite close to what one obtains in a momentum-space analysis, as has been shown in Ref. [67]. In this work, we find that inelastic scattering is sensitive to the increased repulsion of $t_{00}^{C \text{ Breit}}$, but that this feature is also one of the reasons why the IA2 effective interaction does not provide as good a description of data for $E_p < 400$ MeV as the EEI interaction. Optimal factorization is expected to be less reliable at high q than

full folding — our results suggest that the latter may be needed for low energies.

Because the enhanced repulsion at high q implied by Eq. (17) is attributed to Breit-frame kinematics, we have also considered the correct energy at which the t matrix should be evaluated in the Breit frame. As a result, the IA2 effective interactions are evaluated in this work using a q -dependent energy, which follows from placing the $(A-1)$ spectator nucleons on the mass shell. Working in the nucleon-nucleus Breit frame, the invariant mass W for an NN interaction is given by

$$W^2(q) = (E_1 + E_2)^2 - (\mathbf{p}_1 + \mathbf{p}_2)^2 \quad (19)$$

where (E_1, \mathbf{p}_1) and (E_2, \mathbf{p}_2) are the four-momenta of the projectile and struck nucleon, respectively. With the residual nucleus on shell, the energy of the struck nucleon is just the difference

$$E_2 = \sqrt{(Am)^2 + \mathbf{p}_1^2} - \sqrt{(A-1)^2 m^2 + (\mathbf{p}_1 + \mathbf{p}_2)^2}, \quad (20)$$

where $\mathbf{p}_2 = -\mathbf{q}/2 - \mathbf{p}_1/A$ is the momentum for optimal factorization of the NN t matrix. The laboratory energy for free NN scattering has invariant mass

$$W^2 = 2m^2 + 2mE_L. \quad (21)$$

Thus, Eq. (21) implies that the q -dependent effective energy which is used to calculate the NN interaction should be identified as

$$E_L^{\text{eff}}(q) = \frac{W^2(q) - 2m^2}{2m}, \quad (22)$$

where $W(q)$ is obtained from Eqs. (19) and (20). This effective energy is larger than E_L but smaller than E_{Breit} . The effective energy of Eq. (22) is included in our calculations by using t matrices at 50 MeV intervals and interpolating linearly between neighboring energies to arrive at the t matrix with energy $E_L^{\text{eff}}(q)$. The net effect of using the q -dependent energy is to reduce the repul-

sive effect upon $\text{Re}t_{00}^C$ due to E_{Breit}/m by about 10%, but this change has very little effect upon the scattering calculations. We conclude that the increased repulsion implied by Breit-frame kinematics cannot be avoided in an optimal factorization approach.

We also find that recoil corrections to the IA2 effective interaction can have an appreciable effect upon scattering calculations. For example, in Fig. 24 we compare 318 MeV elastic scattering calculations for ^{16}O and ^{40}Ca using the interaction appropriate to each nucleus (solid lines) with calculations using the inappropriate interaction (dashed lines). In other words, the dashed lines for ^{16}O are based upon the interaction for ^{40}Ca , whereas for ^{40}Ca the dashed lines are based upon the interaction for ^{16}O . At this energy the ^{16}O interaction appears to give the best description of the data for both nuclei, including ^{40}Ca . Also note that empirical effective interactions fitted to data for either ^{16}O or ^{40}Ca give a better description of the data for the other nucleus than might be expected from the differences between the solid and dashed lines in Fig. 24. Apparently the differences between the effective interactions for finite nuclei are overestimated by the optimal-factorization prescription.

Improved treatment of the off-shell properties of the invariant amplitudes requires a full-folding calculation, which is beyond the scope of the present work. Furthermore dispersive effects of the mean field upon the collision kinematics also can affect the balance between scalar and vector interactions appreciably. Nonrelativistic G -matrix calculations attempt to include these effects on the propagator self-consistently and find them important in constructing the effective interaction. Similarly, Ray finds that binding potentials give an important repulsive contribution to the real central interaction that decreases quite slowly with energy [8]. Although the IA2 interaction appears to have too much repulsion already, modification of the intermediate states or short-range modification of the pair wave function in nuclear matter might dampen the relativistic effects. It might also be necessary to treat the difference between scalar and

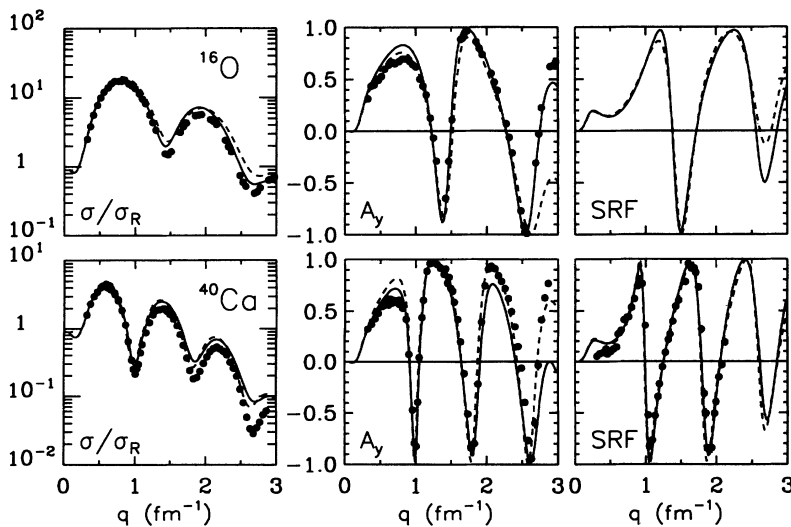


FIG. 24. Sensitivity of elastic scattering calculations at 318 MeV to recoil corrections to the IA2 effective interaction. Solid lines use the interaction appropriate to each nucleus, whereas dashed lines for ^{16}O (^{40}Ca) use the interaction appropriate to ^{40}Ca (^{16}O).

vector densities for inelastic scattering more accurately.

Brown and collaborators have speculated that the effective masses of the mesons which mediate the NN interaction might be modified in the nuclear medium and have performed calculations for proton scattering in which these effective masses depend upon local density [68–70]. Attempts to fit the tensor interaction to scattering data for stretched transitions have also been motivated by this idea [71]. However, none of these calculations have considered the dependence of all components of the nucleon-nucleon interaction upon meson masses in a consistent and systematic manner. The IA2 model, which is based upon a relativistic boson exchange interaction, could provide a framework for systematic investigations of this kind, while including more conventional medium modifications simultaneously. It would be interesting to determine whether density-dependent modification of the meson fields can improve the agreement with the empirical effective interaction.

VI. SUMMARY AND CONCLUSIONS

Calculations based on the IA2 effective interaction, extended to include Pauli blocking and to cover a wider range of projectile energy, are performed for elastic scattering using the Schrödinger equation. The results reproduce those obtained using the IA2 model and the Dirac equation. This interaction has no adjustable parameters for fitting nucleon-nucleus scattering data. More importantly, the IA2 effective interaction provides a means of performing calculations for inelastic scattering which include relativistic dynamics in a nonrelativistic framework. Thus we can take advantage of more advanced nonrelativistic models of nuclear structure or can employ transition densities from electron scattering to minimize uncertainties due to nuclear structure. The latter approach was used to compare the density dependence of the IA2 effective interaction with that of nonrelativistic and empirical models for normal-parity isoscalar transitions sensitive to the central and spin-orbit components of the effective interaction.

The primary source of density dependence in the IA2 effective interaction is provided by the distortion of Dirac spinors, a mechanism not included in nonrelativistic calculations based upon the G matrix. The dominant effect of relativistic density dependence can be described as a short-ranged repulsive contribution to the real central interaction that is proportional to density and nearly independent of energy. This effect is similar to the density dependence of the corresponding component of the empirical effective interaction fitted to data for $E_p > 300$ MeV, but is much stronger than obtained from either the empirical interaction or the G matrix for energies below 200 MeV. In addition, Pauli blocking damps the absorptive potential for energies below 300 MeV and this effect

is similar to that obtained from nonrelativistic models. The density dependence of the IA2 effective interaction is stronger for inelastic than for elastic scattering due to the distortion of an additional spinor. This effect approximately doubles the density dependence of the real parts of the central and spin-orbit interactions, in qualitative agreement with a more schematic model due to Cheon, but has little effect on the imaginary central interaction, contrary to the Cheon model. Furthermore, the enhanced absorption found with empirical effective interactions above 300 MeV is not present in the IA2 elastic interaction, but the corresponding inelastic interaction is enhanced. If these characteristics remain after correction of the IA2 model for self-consistent modifications of the propagator and the intermediate states, as prescribed by the G matrix, the use of the Cheon rearrangement factor in data analysis will have to be reevaluated.

The density dependence of the IA2 effective interaction is too strong at low energy to reproduce the inelastic scattering data. Better agreement with the data, and with the empirical effective interaction, is obtained at 318 MeV. By 500 MeV the IA2 model is in good agreement with both the data and the empirical effective interaction, whereas the nonrelativistic theory of the effective interaction fails to predict adequate density dependence. Apparently the nonrelativistic models would benefit from inclusion of relativistic effects for energies above 300 MeV, provided that the energy dependence of these effects is modified so that results closer to the nonrelativistic models are obtained at low energy.

The success of the empirical effective interaction in reproducing data for many transitions among several nuclei simultaneously demonstrates that the effective interaction depends primarily upon local density and is essentially independent of either state or nucleus. However, that approach cannot differentiate between conventional medium modifications, such as Pauli blocking and dispersion, or relativistic effects due to the distortion of Dirac spinors, or off-shell and nonlocal effects due to full folding [72–74]. Further insight into the proper interpretation of the empirical effective interaction awaits the development of a detailed theoretical model capable of including Pauli blocking, dispersion, relativistic dynamics, and NN inelasticity in a self-consistent model of the effective interaction for finite nuclei. Work on inclusion of dispersive effects in the IA2 model is in progress.

ACKNOWLEDGMENTS

The authors thank Professor John Tjon for supplying Pauli-blocked t matrices which are used in this work. The support of the U.S. Department of Energy under Grant No. DE-FG05-87ER-40322 and the National Science Foundation under Grant No. PHY-9220690 is gratefully acknowledged.

- [1] J. P. Jeukenne, A. Lejeune, and C. Mahaux, *Phys. Rev. C* **10**, 1391 (1974).
- [2] J. P. Jeukenne, A. Lejeune, and C. Mahaux, *Phys. Rep.* **25**, 83 (1976); *Phys. Rev. C* **15**, 10 (1977); **16**, 80 (1977).
- [3] F. A. Brieva and J. R. Rook, *Nucl. Phys.* **A291**, 299 (1977); **A291**, 317 (1977); **A297**, 206 (1978); **A307**, 493 (1978).
- [4] H. V. von Geramb, F. A. Brieva, and J. R. Rook, in *Microscopic Optical Potentials*, edited by H. V. von Geramb (Springer-Verlag, Berlin, 1979), p. 104.
- [5] H. V. von Geramb, in *The Interaction Between Medium Energy Nucleons in Nuclei—1982*, edited by H. O. Meyer, AIP Conf. Proc. No. 97 (AIP, New York, 1983), p. 44.
- [6] L. Rikus, K. Nakano, and H. V. von Geramb, *Nucl. Phys.* **A414**, 413 (1984).
- [7] K. Nakayama and W. G. Love, *Phys. Rev. C* **38**, 51 (1988).
- [8] L. Ray, *Phys. Rev. C* **41**, 2816 (1990).
- [9] L. G. Arnold, B. C. Clark, R. L. Mercer, and P. Schwandt, *Phys. Rev. C* **23**, 1949 (1981); L. G. Arnold, B. C. Clark, and R. L. Mercer, *ibid.* **23**, 15 (1981); B. C. Clark, R. L. Mercer, and P. Schwandt, *Phys. Lett.* **122B**, 211 (1983).
- [10] S. Hama, B. C. Clark, E. D. Cooper, H. S. Sherif, and R. L. Mercer, *Phys. Rev. C* **41**, 2737 (1990).
- [11] E. D. Cooper, S. Hama, B. C. Clark, and R. L. Mercer, *Phys. Rev. C* **47**, 297 (1993).
- [12] J. A. McNeil, J. R. Shepard, and S. J. Wallace, *Phys. Rev. Lett.* **50**, 1439 (1983).
- [13] J. R. Shepard, J. A. McNeil, and S. J. Wallace, *Phys. Rev. Lett.* **50**, 1443 (1983).
- [14] J. A. McNeil, L. Ray, and S. J. Wallace, *Phys. Rev. C* **27**, 2123 (1983).
- [15] B. C. Clark, S. Hama, R. L. Mercer, L. Ray, and B. D. Serot, *Phys. Rev. Lett.* **50**, 1644 (1983); B. C. Clark, S. Hama, R. L. Mercer, L. Ray, G. W. Hoffmann, and B. D. Serot, *Phys. Rev. C* **28**, 1421 (1983).
- [16] M. V. Hynes, A. Picklesimer, P. C. Tandy, and R. M. Thaler, *Phys. Rev. Lett.* **52**, 978 (1984); M. V. Hynes, A. Picklesimer, P. C. Tandy, and R. M. Thaler, *Phys. Rev. C* **31**, 1438 (1985).
- [17] J. A. Tjon and S. J. Wallace, *Phys. Rev. C* **36**, 280 (1987).
- [18] J. A. Tjon and S. J. Wallace, *Phys. Rev. C* **36**, 1085 (1987).
- [19] N. Ottenstein, S. J. Wallace, and J. A. Tjon, *Phys. Rev. C* **38**, 2272 (1988); **38**, 2289 (1988).
- [20] D. P. Murdock and C. J. Horowitz, *Phys. Rev. C* **35**, 1442 (1987).
- [21] B. C. Clark, S. Hama, E. Sugarbaker, M. A. Franey, R. L. Mercer, L. Ray, G. W. Hoffmann, and B. D. Serot, *Phys. Rev. C* **30**, 314 (1984).
- [22] J. R. Shepard, E. Rost, and J. A. McNeil, *Phys. Rev. C* **33**, 634 (1986).
- [23] D. Frekers, S. S. M. Wong, R. E. Azuma, T. E. Drake, J. D. King, L. Buchmann, R. Schubank, R. Abegg, K. P. Jackson, C. A. Miller, S. Yen, W. P. Alford, R. L. Helmer, C. Broude, S. Mattson, and E. Rost, *Phys. Rev. C* **35**, 2236 (1987).
- [24] K. H. Hicks, R. G. Jeppesen, C. C. K. Lin, R. Abegg, K. P. Jackson, O. Häusser, J. Lisannti, C. A. Miller, E. Rost, R. Sawafra, M. C. Vetterli, and S. Yen, *Phys. Rev. C* **38**, 229 (1988).
- [25] E. Rost, J. R. Shepard, E. R. Siciliano, and J. A. McNeil, *Phys. Rev. C* **29**, 209 (1984).
- [26] V. K. Mishra, B. C. Clark, E. D. Cooper, and R. L. Mercer, *Phys. Rev. C* **41**, 370 (1990).
- [27] S. Shim, B. C. Clark, E. D. Cooper, S. Hama, R. L. Mercer, L. Ray, J. Raynal, and H. S. Sherif, *Phys. Rev. C* **42**, 1592 (1990).
- [28] R. J. Furnstahl and S. J. Wallace, *Phys. Rev. C* **47**, 2812 (1993).
- [29] J. J. Kelly, in *Perspectives in Nuclear Physics at Intermediate Energies*, edited by S. Boffi, C. C. degli Atti, and M. Giannini (World Scientific, Singapore, 1992), p. 197.
- [30] T. Cheon, K. Takayanagi, and K. Yazaki, *Nucl. Phys.* **A437**, 301 (1985); **A445**, 227 (1985).
- [31] T. Cheon and K. Takayanagi, *Nucl. Phys.* **A455**, 653 (1986).
- [32] L. Ray, *Phys. Rev. C* **47**, 2990 (1993).
- [33] J. J. Kelly, W. Bertozzi, T. N. Buti, J. M. Finn, F. W. Hersman, C. Hyde-Wright, M. V. Hynes, M. A. Kovash, B. Murdock, B. E. Norum, B. Pugh, F. N. Rad, A. D. Bacher, G. T. Emery, C. C. Foster, W. P. Jones, D. W. Miller, B. L. Berman, W. G. Love, J. A. Carr, and F. Petrovich, *Phys. Rev. C* **39**, 1222 (1989).
- [34] J. J. Kelly, *Phys. Rev. C* **39**, 2120 (1989).
- [35] J. J. Kelly, W. Bertozzi, T. N. Buti, J. M. Finn, F. W. Hersman, C. Hyde-Wright, M. V. Hynes, M. A. Kovash, B. Murdock, P. Ulmer, A. D. Bacher, G. T. Emery, C. C. Foster, W. P. Jones, D. W. Miller, and B. L. Berman, *Phys. Rev. C* **41**, 2504 (1990); Q. Chen, J. J. Kelly, P. P. Singh, M. C. Radhakrishna, W. P. Jones, and H. Nann, *ibid.* **41**, 2514 (1990); J. J. Kelly, Q. Chen, P. P. Singh, M. C. Radhakrishna, W. P. Jones, and H. Nann, *ibid.* **41**, 2525 (1990).
- [36] H. Seifert, J. J. Kelly, A. E. Feldman, B. S. Flanders, M. A. Khandaker, Q. Chen, A. D. Bacher, G. P. A. Berg, E. J. Stephenson, P. Karen, B. E. Norum, P. Welch, and A. Scott, *Phys. Rev. C* **47**, 1615 (1993).
- [37] J. J. Kelly, A. E. Feldman, B. S. Flanders, H. Seifert, D. Lopiano, B. Aas, A. Azizi, G. Igo, G. Weston, C. Whitten, A. Wong, M. V. Hynes, J. McClelland, W. Bertozzi, J. M. Finn, C. E. Hyde-Wright, R. W. Lourie, P. E. Ulmer, B. E. Norum, and B. L. Berman, *Phys. Rev. C* **43**, 1272 (1991).
- [38] J. J. Kelly, P. Boberg, A. E. Feldman, B. S. Flanders, M. A. Khandaker, S. D. Hyman, H. Seifert, P. Karen, B. E. Norum, P. Welch, S. Nanda, and A. Saha, *Phys. Rev. C* **44**, 2602 (1991).
- [39] B. S. Flanders, J. J. Kelly, H. Seifert, D. Lopiano, B. Aas, A. Azizi, G. Igo, G. Weston, C. Whitten, A. Wong, M. V. Hynes, J. McClelland, W. Bertozzi, J. M. Finn, C. E. Hyde-Wright, R. W. Lourie, B. E. Norum, P. E. Ulmer, and B. L. Berman, *Phys. Rev. C* **43**, 2103 (1991).
- [40] M. A. Khandaker, J. J. Kelly, P. Boberg, A. E. Feldman, B. S. Flanders, S. Hyman, H. Seifert, P. Karen, B. E. Norum, P. Welch, S. Nanda, and A. Saha, *Phys. Rev. C* **44**, 1978 (1991).
- [41] W. G. Love and M. A. Franey, *Phys. Rev. C* **24**, 1073 (1981).
- [42] M. A. Franey and W. G. Love, *Phys. Rev. C* **31**, 488 (1985).
- [43] M. Lacombe, B. Loiseau, J. M. Richard, R. Vinh Mau, J. Cote, P. Pires, and R. de Tourreil, *Phys. Rev. C* **21**, 861 (1980).
- [44] P. J. Siemens, *Nucl. Phys.* **A141**, 225 (1970).

- [45] R. Machleidt, K. Holinde, and Ch. Elster, *Phys. Rep.* **149**, 1 (1987).
- [46] E. L. Lomon and H. Feshbach, *Ann. Phys. (N.Y.)* **48**, 94 (1968).
- [47] E. L. Lomon, *Phys. Rev. D* **26**, 576 (1982).
- [48] L. Ray, *Phys. Rev. C* **35**, 1072 (1987).
- [49] E. Clementel, and C. Villi, *Nuovo Cimento* **2**, 176 (1955).
- [50] R. A. Arndt, L. D. Roper, R. A. Bryan, R. B. Clark, B. J. VerWest, and P. Signell, *Phys. Rev. D* **32**, 128 (1987); R. A. Arndt, J. S. Hyslop III, and L. D. Roper, *ibid.* **35**, 128 (1987); R. A. Arndt and L. D. Roper, *Scattering Analysis Interactive Dial-in SAID* (Virginia Polytechnic Institute, Blacksburg, 1988).
- [51] A. K. Kerman, H. McManus, and R. M. Thaler, *Ann. Phys.* **8**, 551 (1959).
- [52] G. Lahm, Ph.D. thesis, University of Mainz, 1982.
- [53] H. J. Emrich, Ph.D. thesis, University of Mainz, 1983.
- [54] H. deVries, C. W. deJager, and C. deVries, *At. Data Nucl. Data Tables* **36**, 495 (1987).
- [55] J. Dechargé and D. Gogny, *Phys. Rev. C* **21**, 1568 (1980).
- [56] L. Ray and G. W. Hoffmann, *Phys. Rev. C* **31**, 538 (1985); L. Ray, private communication.
- [57] E. J. Stephenson, *J. Phys. Soc. Jpn. (Suppl.)* **55**, 316 (1985); P. Schwandt, private communication.
- [58] E. Belszynski, B. Aas, D. Adams, M. Bleszynski, G. J. Igo, T. Jaroszewicz, A. Ling, D. Lopiano, F. Sperisen, M. G. Moshi, C. A. Whitten, K. Jones, and J. B. McClelland, *Phys. Rev. C* **37**, 1527 (1988).
- [59] G. W. Hoffmann, L. Ray, M. L. Barlett, R. Ferguson, J. McGill, E. C. Milner, K. K. Seth, D. Barlow, M. Bosko, S. Iversen, M. Kaletka, A. Saha, and D. Smith, *Phys. Rev. Lett.* **47**, 1436 (1981).
- [60] F. Petrovich, R. J. Philpott, A. W. Carpenter, and J. A. Carr, *Nucl. Phys.* **A425**, 609 (1984).
- [61] F. Petrovich, J. A. Carr, R. J. Philpott, A. W. Carpenter, and J. Kelly, *Phys. Lett.* **165B**, 19 (1985).
- [62] T. N. Buti, J. J. Kelly, W. Bertozzi, J. M. Finn, F. W. Hersman, C. Hyde-Wright, M. V. Hynes, M. A. Kovash, S. J. Kowalski, R. W. Lourie, B. Murdock, B. E. Norum, B. Pugh, C. P. Sargent, W. Turchinets, and B. L. Berman, *Phys. Rev. C* **33**, 755 (1986).
- [63] R. A. Miskimen, Ph.D. thesis, Massachusetts Institute of Technology, 1983.
- [64] K. K. Seth, D. Barlow, A. Saha, R. Soundranyagam, S. Iversen, M. Kaletka, M. Basko, D. Smith, G. W. Hoffmann, M. L. Barlett, R. Ferguson, J. McGill, and E. C. Miller, *Phys. Lett.* **158B**, 23 (1985).
- [65] J. Lisantti, D. J. Horen, F. E. Bertrand, R. L. Auble, B. L. Burks, E. E. Gross, R. O. Sayer, D. K. McDaniels, K. W. Jones, J. B. McClelland, S. J. Seestrom-Morris, and L. W. Swenson, *Phys. Rev. C* **39**, 569 (1989).
- [66] B. Aas, E. Bleszynski, M. Bleszynski, M. Hajisaeid, G. J. Igo, F. Irom, G. Pauletta, A. Rahbar, A. T. M. Wang, J. F. Amann, T. A. Carey, W. D. Cornelius, and J. B. McClelland, *Nucl. Phys.* **A460**, 675 (1986).
- [67] N. Ottenstein, E. E. Faassen, J. A. Tjon, and S. J. Wallace, *Phys. Rev. C* **43**, 2393 (1991).
- [68] G. E. Brown, C. B. Dover, P. B. Siegel, and W. Weise, *Phys. Rev. Lett.* **60**, 2723 (1988).
- [69] G. E. Brown and M. Rho, *Phys. Rev. Lett.* **66**, 2720 (1991).
- [70] G. E. Brown, A. Sethi, and N. M. Hintz, *Phys. Rev. C* **44**, 2653 (1991).
- [71] H. Baghaei, R. A. Lindgren, P. Slocum, E. J. Stephenson, A. D. Bacher, S. Chang, J. Lisantti, J. Lui, C. Olmer, S. Wells, S. W. Wissink, B. Clausen, J. Carr, and F. Petrovich, *Phys. Rev. Lett.* **69**, 2054 (1992).
- [72] H. F. Arellano, F. A. Brieva, and W. G. Love, *Phys. Rev. C* **41**, 2188 (1990).
- [73] Ch. Elster, T. Cheon, E. F. Redish, and P. C. Tandy, *Phys. Rev. C* **41**, 814 (1990).
- [74] R. Crespo, R. C. Johnson, and J. A. Tostevin, *Phys. Rev. C* **41**, 2257 (1990).

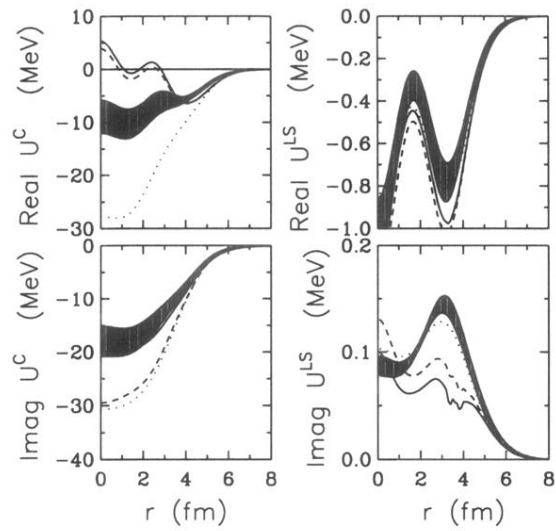


FIG. 7. Optical potentials for ^{40}Ca at 200 MeV. The bands represent the spread among several empirical effective interactions fitted to data for elastic and inelastic scattering for ^{16}O and/or ^{40}Ca . The dotted lines omit density dependence, the dashed lines include relativistic corrections, and the solid lines include Pauli blocking corrections based upon the IA2 model.

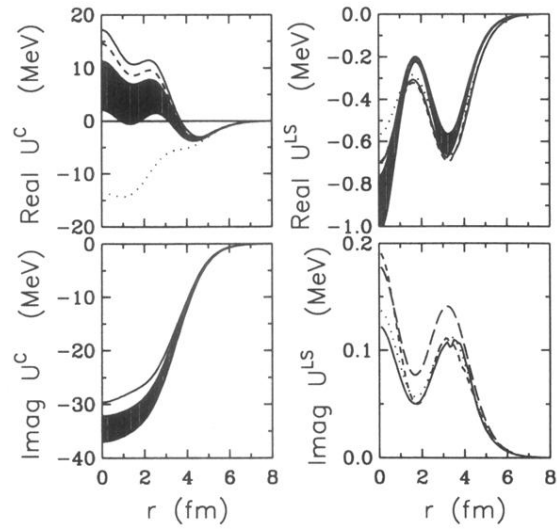


FIG. 8. Optical potentials for ^{40}Ca at 318 MeV. The bands represent the spread among several empirical effective interactions fitted to data for elastic and inelastic scattering for ^{16}O and/or ^{40}Ca . The long-dashed curve for $\text{Im}U^{LS}$ was used with the EEI model. The dotted lines omit density dependence, the dashed lines include relativistic corrections, and the solid lines include Pauli blocking corrections based upon the IA2 model.

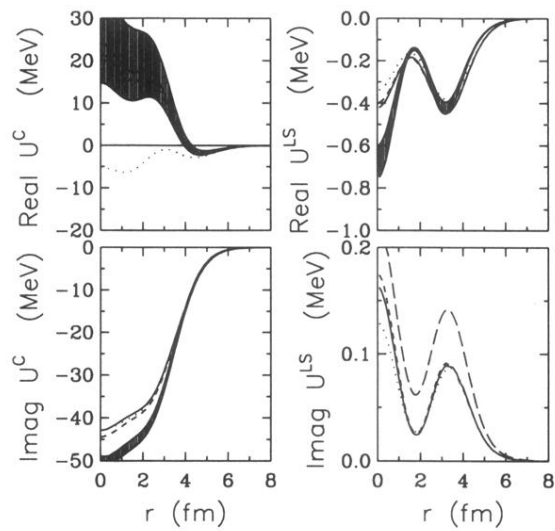


FIG. 9. Optical potentials for ^{40}Ca at 500 MeV. The bands represent the spread among several empirical effective interactions fitted to data for elastic and inelastic scattering for ^{16}O and/or ^{40}Ca . The long-dashed curve for $\text{Im}U^{LS}$ was used with the EEI model. The dotted lines omit density dependence, the dashed lines include relativistic corrections, and the solid lines include Pauli blocking corrections based upon the IA2 model.